Proton radiography to reduce range uncertainty in proton therapy

Sylvain Deffet

Institute of Information and Communication Technologies, Electronics and Applied Mathematics (ICTEAM)
Université catholique de Louvain

A thesis submitted in partial fulfillment of the requirements for the degree of
Doctor in Applied Sciences

November 27, 2018

During this thesis, Sylvain Deffet was supported by a research grant from Ion Beam Applications (IBA s.a.).

PhD committee

Thesis supervisor

Prof. Benoît Macq, PhD, Ir
Institute of Information and Communication Technologies, Electronics and Applied Mathematics, Université catholique de Louvain
École polytechnique de Louvain, Université catholique de Louvain

President of the jury

Prof. Jean-Pierre Raskin, PhD, Ir
Institute of Information and Communication Technologies, Electronics and Applied Mathematics, Université catholique de Louvain
École polytechnique de Louvain, Université catholique de Louvain

Members

Prof. Denis Flandre, PhD, Ir
Institute of Information and Communication Technologies, Electronics and Applied Mathematics, Université catholique de Louvain
École polytechnique de Louvain, Université catholique de Louvain

Dr. Rudi Labarbe, PhD
Ion Beam Applications SA (IBA), Louvain-la-Neuve

Prof. John A. Lee, PhD, Ir
Molecular Imaging, Radiotherapy and Oncology, Université catholique de Louvain
École polytechnique de Louvain, Université catholique de Louvain

Prof. Edmond Sterpin, PhD, Ir
Molecular Imaging, Radiotherapy and Oncology, Université catholique de Louvain
Laboratory of Experimental Radiotherapy, Katholieke Universiteit Leuven

Invited member

Prof. Philippe Lambin, PhD
The D-Lab: Decision Support for Precision Medicine, University of Maastricht
Maastricht University Medical Center
The Netherlands

Abstract

Proton therapy is an advanced form of radiation therapy which is increasingly used worldwide. Unlike photons, protons deliver a sharp dose at a precise location corresponding to their range in the patient. Thanks to this physical property, proton therapy has the potential to spare healthy tissues better than conventional radiation therapy. However, a consequence of this dosimetric property is that the range of the protons inside the patient must be accurately predicted to deliver the dose as planned. Unfortunately, several uncertainties arising during treatment planning may significantly impact the range of the protons and hence jeopardize dose conformity. To better quantify and potentially reduce the uncertainties, the implementation of imaging techniques that would provide a direct information on the energy reduction of protons in the patient is highly desirable. In the present thesis, such a method is introduced: proton radiography. The system that we propose relies on the use of protons having an energy high enough for them to traverse the patient and stop inside a detector which measures their residual range. By comparing measured and predicted residual ranges, it is possible to quantify range uncertainties in the patient in clinical conditions.

Although the principle of proton radiography is relatively straightforward, a clinical implementation of such a measurement device is a complex issue. This thesis aims at developing a proton radiography system and also at conceiving an acquisition process that could be conveniently implemented in clinics. The methodologies to correctly take advantage of proton radiography measurements are also discussed, in order to further optimize the dose delivered to the patient and improve *de facto* the treatment outcome.

Acknowledgments

My acknowledgments are first addressed to my supervisor, Prof. Benoît Macq (Université catholique de Louvain, Belgium) for having welcomed me in such a wonderful research environment. Thanks to his support, guidance, and the freedom he gave me in the development of my work, this scientific journey has been a great personal development.

I would also like to show my appreciation to my PhD committee Prof. Denis Flandre (UCLouvain), Dr. Rudi Labarbe (Ion Beam Applications, Belgium), and Prof. John Lee (UCLouvain) for their coaching and advices. In addition, I would like to thank the entire PhD jury, composed of the PhD committee and three additional members, Prof. Edmond Sterpin (UCLouvain and Katholieke Universiteit Leuven, Belgium), Prof. Philippe Lambin (Maastricht University, The Netherlands) and Prof. Jean-Pierre Raskin (UCLouvain). I wish to extend a special thank to Prof. Edmond Sterpin and Dr. Rudi Labarbe for the time spent guiding me through the improvement of this manuscript. Thank you for the interesting discussions and your numerous judicious comments.

I thank very much François Vander Stappen (IBA) who guided me during most of this thesis. Your enthusiasm was contagious and your wise recommendations were very inspiring. It was always with a great pleasure and interest that I travelled with you to discuss ~~problems~~ solutions with our partners. I am also thankful to Antoine Pouppez (IBA) for his management during the second part of this project.

During my PhD, I really enjoyed working at the ImagX.R lab which is a mixed team of industrial and scientific members from IBA and UCLouvain. A special thank is due to Rudi Labarbe for having contributed so much to make it an ideal research environment by continuously enforcing the collaboration with IBA and sharing his time to support our work. I

also thank all my colleagues at ImagX.R, MIRO and IBA who also contributed to this friendly and productive atmosphere: Yafei, Jaroslav, Damien, Florence, Valérie, Gaëtan, Jean, Eliott, Mérence, Arnould, Kevin, Marie, Ana, Guillaume, Lucian, Arnaud, Julien and many others.

Most of this work was done in partnership with medical physicists of the Proton Therapy Center of Trento (Italy). I thank Dr Paolo Farace and Dr Roberto Righetto very much for the numerous exchanges of great ideas and suggestions. You welcomed me in Trento at the beginning of my PhD and this was the trigger of a marvelous scientific journey.

I would like to gratefully acknowledge the financial and non-financial supports received from Ion Beam Applications who gave me the ability to achieve this work.

Finally, I reserve special praise for my parents Marie-Paule and Michel, for my brother Olivier, and for Sophie for their unwavering support and for being always so joyful to start a mathematical discussion.

List of publications

Articles in peer-reviewed journals and peer-reviewed proceedings

A direct ray-tracing method to compute integral depth dose in pencil beam proton radiography with multilayer ionization chamber
P Farace, R Righetto, S Deffet, A Meijers, F Vander Stappen
Medical physics 43 (12), 6405-6412

Registration of pencil beam proton radiography data with X-ray CT
S Deffet, B Macq, R Righetto, F Vander Stappen, P Farace
Medical physics 44 (10), 5393-5401

Water equivalent thickness estimation via sparse deconvolution of proton radiography data
S Deffet, B Macq, F Vander Stappen, P Farace
IEEE International Conference on Acoustics, Speech and Signal Processing (ICASSP) 2018

Conference communications

Pencil beam proton radiography using a multilayer ionization chamber
S Deffet, P Farace, R Righetto, F Vander Stappen
Proton therapy co-operative group (PTOCG) annual meeting 2016, Prague, Czech Republic

Pencil beam proton radiography using a multilayer ionization chamber
S Deffet, P Farace, R Righetto, F Vander Stappen
IBA annual users meeting 2016, Trento, Italy

SU-G-TeP2-13: Patient-Specific Reduction of Range Uncertainties in Proton Therapy by Proton Radiography with a Multi-Layer Ionization Chamber
S Deffet, P Farace, R Righetto, B Macq, F Vander Stappen
Fifty-eighth annual meeting of the american association of physicists in medicine 2017, Washington DC, USA

Status of the development of a proton imaging system
S Deffet, P Farace, F Vander Stappen, B Macq
Réunion du GdR ISIS : Co-conception : capteurs hybrides et algorithmes pour des systèmes innovants 2017, Paris, France

Status of the development of a proton imaging system
S Deffet, P Farace, F Vander Stappen, B Macq
Belgian Hospital Physicists Association (BHPA) Symposium 2018, Charleroi, Belgium

Water Equivalent Thickness Estimation via Sparse Deconvolution of Proton Radiography Data S Deffet, B Macq, F Vander Stappen, P Farace
IEEE International Conference on Acoustics, Speech and Signal Processing (ICASSP) 2018, Calgary, Canada

Acronyms

CT	Computed tomography
CSDA	Continuous slowing down approximation
DTA	Distance to agreement
Hi	Heterogeneity index
HU	Hounsfield unit
IBA	Ion Beam Applications S.A.
IDD	Integral depth dose
IMPT	Intensity modulated proton therapy
IMRT	Intensity modulated radiation therapy
MCS	Multiple Coulomb scattering
MLIC	Multi-layer ionization chamber
MU	Monitor unit
NTCP	Normal tissue complication probability
PCB	Printed circuit board
QA	Quality assurance
PBS	Pencil beam scanning
PR	Proton radiograph(y)
RD	Range difference

RE	Range error
RSP	Relative stopping power
SDD	Standard deviation of differences
SOBP	Spread-out Bragg peak
SPR	Stopping power ratio
TCP	Tumor control probability
TPS	Treatment planning system
UCLouvain	Université catholique de Louvain
WEPL	Water equivalent path length
WET	Water equivalent thickness

Contents

Chapter 1

Range uncertainty in proton therapy

1.1 Proton therapy

1.1.1 Rationale of proton therapy

Cancer is, according to the World Health Organization (WHO), the second leading cause of death in the world. This type of disease is characterized by the uncontrolled growth of abnormal cells. It can affect any kind of organs and spread to other locations, creating metastases. Depending on the diagnostic outcome, various treatment types may be considered: surgery, radiotherapy, chemotherapy, ... Estimates show that approximately fifty percents of patients having a cancer would benefit from radiotherapy [48, 6]. This technique is based on the use of radiation to damage cancerous cells by ionization processes. In this context, the aim of treatment planning is to maximize the dose received by the tumor and to minimize the one collaterally given to healthy tissues. In other words, it is a matter of reaching a high probability of local control of the tumor (tumor control probability, TCP) and a low probability of complications in normal tissues (normal tissue complication probability, NTCP).

The vast majority of radiotherapy treatments rely on the use of photons. Nonetheless, those particles have a dose deposition profile which is essentially a decreasing function of the depth into the matter. Con-

sequently, significant dose is deposited on the way to the target and, to a lower extent, downstream. To better confine most of the dose to the tumor solely, conventional radiotherapy has benefited from extensive developments over the past decades. In the first instance, intensity modulated radiotherapy (IMRT) was developed to deliver beams with distinct intensities and geometrical shapes at determined angles [52]. More recently, helical tomotherapy extended the potential of IMRT by delivering such treatments for a large number of arcs in very limited amount of time.

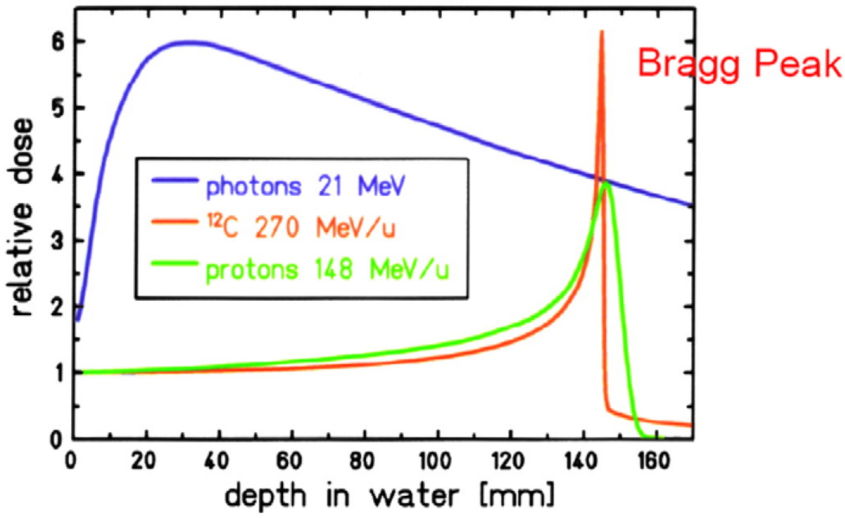

Figure 1.1: Depth-dose deposition profiles of photons vs. protons vs. carbon ions. From [20].

Despite the major technological developments achieved in conventional radiotherapy, the characteristic dose deposition profiles of photons is an intrinsic limitation in the continuous quest for lower NTCP. There exists a form of radiation therapy, however, which does not have this limitation and which is increasingly used worldwide: ion therapy. The rationale behind the use of ions of which the most frequently encountered types in clinics are protons, resides in a depth-dose profile characterized by a peak, named the Bragg peak. This is illustrated in Fig. 1.1 which presents a comparison between dose deposition profiles of

photons and two types of ions: protons and carbon ions.

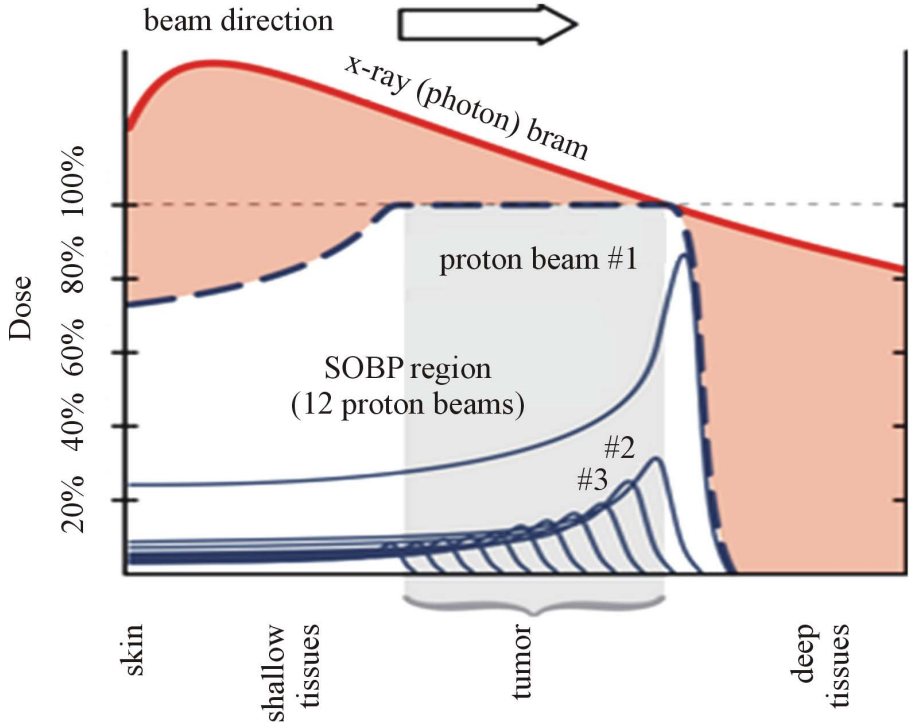

Figure 1.2: Depth-dose deposition profiles of photons vs. protons. A spread-out Bragg peak (SOBP) may be obtained by modulating the initial energy of protons. From [51].

The sharp distal fall-off of the Bragg peak makes it ideal to spare tissues located after the tumor. Moreover, the peak is preceded by a low-dose plateau which may potentially reduce the dose delivered on the way to the tumour. Finally, by modulating the initial energy of protons to form a spread-out Bragg peak (SOBP), most of the dose can be confined to the target volume, as illustrated in Fig. 1.2.

1.1.2 Proton therapy delivery

Bringing protons from the accelerator to the tumour involves the use of a complex system, as illustrated in Fig. 1.3. First, hydrogen atoms

are ionized. The protons generated in this process are then accelerated which may be typically done by a cyclotron. For IBA cyclotrons, the kinetic energy is usually around 230 MeV. This corresponds to a range of 33 cm in water. In the next step, the protons energy may be adjusted to fit the desired range using a degrader. The beam is then directed to the treatment room via a beam line equipped with focusing magnets.

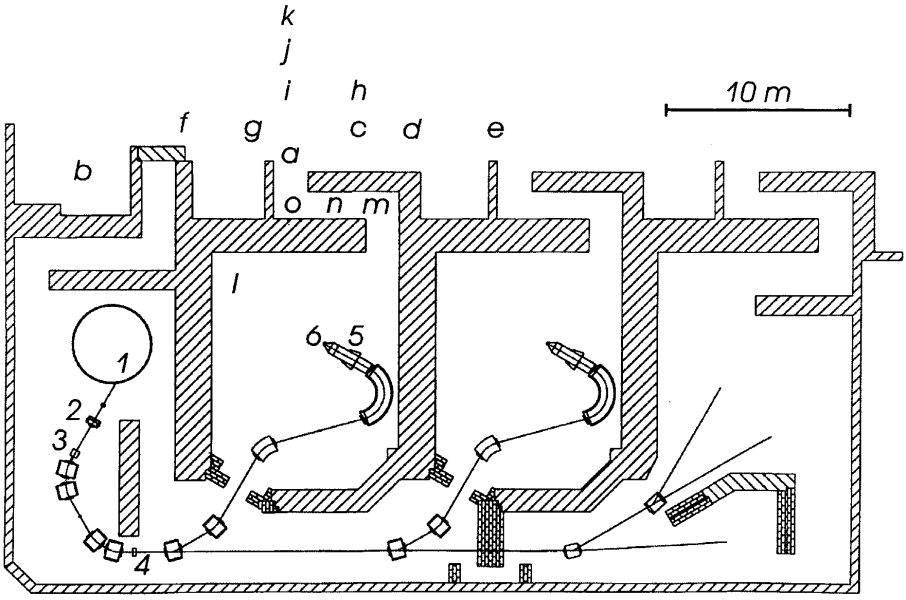

Figure 1.3: Proton therapy facility treatment level: cyclotron (1), energy degrader (2), momentum analysis magnets (3), slits (4), brass aperture (5), beamstop at isocenter (6). Plan also shows the main control room (b), treatment room maze exit (m, n, o, a), and various corridors and occupied rooms on the level above (c–k). From [36].

As we pointed it out in Fig. 1.2, the use of a single energy is not sufficient to cover a tumor all the way from its proximal to distal side. A combination of beams of distinct energies is required in order to form a SOBP. Moreover, the delivered beam must achieve lateral conformity of the prescribed dose. To do so, two main categories of delivery techniques exist. Initially, "passive" methods were employed. They rely on a beam shaping system, typically a collimator which contains a hole shaped according to the tumour. This system has several drawbacks.

The first one is the intrinsic limitation of the distal or proximal dose conformity. Secondly, neutrons are emitted close to the patient because of interactions of protons with the beam shaping system. Finally, collimators must be designed patient specifically which leads to additional cost, QA, and in-room time. To remedy this situation, a second generation of delivery technique called pencil beam scanning (PBS) was developed which works by painting the desired shape for each given energy. This was made possible by the use of scanning magnets which can give the beam an angle, as illustrated in Fig. 1.4.

PBS can deliver complex heterogeneous dose which led to a new treatment technique called intensity modulated proton therapy (IMPT). In this thesis, we only consider this delivery method given the secured trend to replace passive systems with PBS.

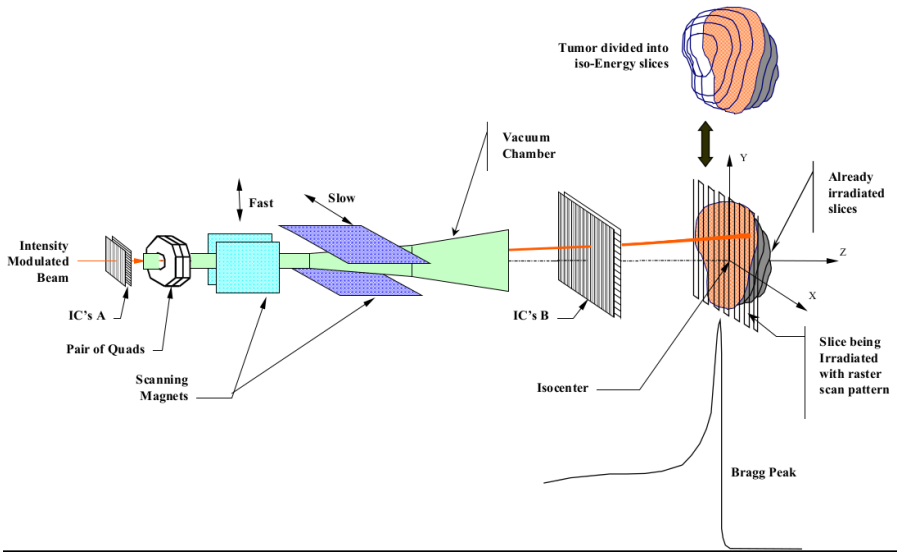

Figure 1.4: Pencil beam scanning using scanning magnets. From [31].

1.1.3 Proton range and treatment planning

The proton range is usually defined as the depth at which half of the protons of the beam come to rest in the medium [35], which in the case of a pristine Bragg peak corresponds to the point where the dose decreases

to 80% of the maximum dose. Nevertheless, other definitions like the 90% fall-off position are sometimes preferred [37]. Another definition commonly used consists in integrating the inverse of the energy loss rate from the initial energy down to rest [35]. It is however an approximation since fluctuations in energy loss arising from the stochastic nature of proton interactions with the medium are neglected. According to this definition called the continuous slowing down approximation (CSDA), the range named R_{CSDA} may be expressed as:

$$R_{CSDA} = \int_{E_0}^{0} \frac{1}{\frac{dE}{dx}} dE \tag{1.1}$$

where E_0 is the initial energy of the protons.

Because of the dependence of the range to the energy loss rate, $\frac{dE}{dx}$ is paramount in proton therapy. The proton stopping power is defined as the opposite of this physical property and is referred to as S:

$$S = -\frac{dE}{dx} \tag{1.2}$$

It is a function of the nature of the encountered material and of the energy of the particle, as illustrated in Fig. 1.5 for a medium composed of water.

Conveniently, the stopping power of tissues is commonly considered relative to water since this physical quantity is almost independent on the energy for the range used in proton therapy. The relative stopping power (RSP) is also sometimes referred to as stopping power ratio (SPR). In this thesis, both names are used interchangeably:

$$RSP = SPR = \frac{S(E)}{S_{water}(E)} \tag{1.3}$$

During treatment planning, the 3D map of the patient's RSP is estimated based on a CT scan which provides an attenuation map of photons. Those data are expressed in Hounsfield units (HU). This image modality is not only useful to compute RSP; it also provides a representation of the patient's anatomy based on which tumor areas and various organs are contoured.

The RSP map and organ contours are prerequisites to the computation of the different beam angles and energy layers that will lead to

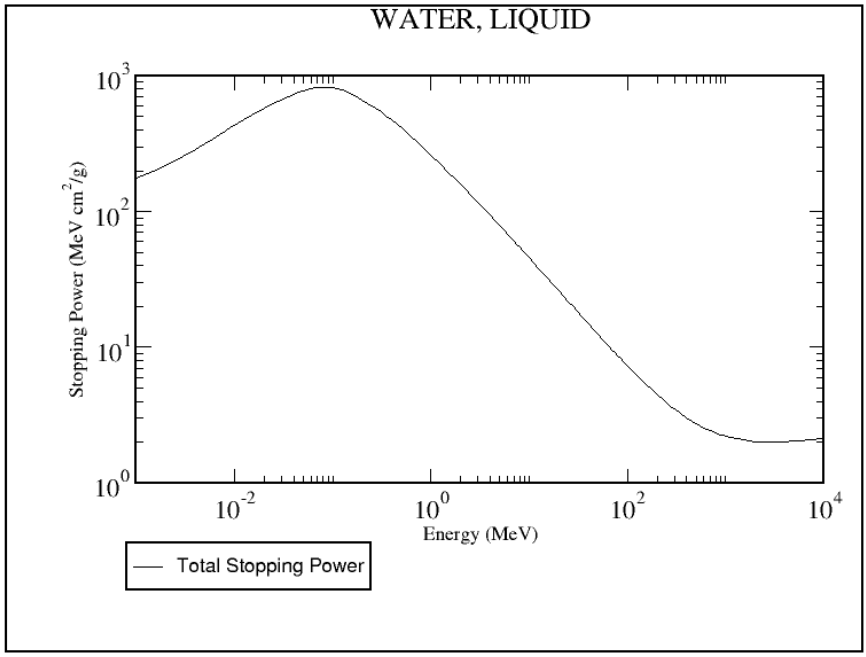

Figure 1.5: Proton stopping power of water vs. proton energy. From the PSTAR database of the National Institute of Standards and Technology, USA.

the delivery of the prescribed dose. To accurately estimate the beam parameters, the dose distribution inside the patient must be modelled. There are two main types of methods: analytical algorithms which rely on macroscopic models and Monte Carlo simulations which model the stochastic interactions of protons within the materials encountered in the patient.

1.2 Range uncertainty in proton therapy

Uncertainties in range prediction are critical: they may result in underdosage of the tumour and over-dosage of surrounding healthy organs. In his widely celebrated paper, Paganetti [37] listed the various sources of

uncertainties taking place during range computation. Those are shown in Table 1.1 which does not include impacts of changes in the patient's anatomy (between treatment fractions), organs motions (during treatment fraction), imaging artifacts and biological effects.

Source of range uncertainty in the patient	Range uncertainty without Monte Carlo	Range uncertainty with Monte Carlo
Independent on dose calculation		
Measurement uncertainty in water for commissioning	±0.3mm	±0.3mm
Compensator design	±0.2mm	±0.2mm
Beam reproducibility	±0.2mm	±0.2mm
Patient setup	±0.7mm	±0.7mm
Dose calculation		
CT imaging and calibration	±0.5%	±0.5%
CT conversion to tissue (excluding I-values)	±0.5%	±0.2%
CT grid size	±0.3%	±0.3%
Mean excitation energy (I-values) in tissues	±1.5%	±1.5%
Range degradation; complex inhomogeneities	−0.7%	±0.1%
Range degradation; local lateral inhomogeneities ∗	±2.5%	±0.1%
Total	4.6% + 1.2mm	2.4% + 1.2mm
Total excluding ∗	2.7% + 1.2mm	2.4% + 1.2mm

Table 1.1: Sources of range uncertainty. From [37].

Table 1.1 unveils two major contributions. First, range degradation caused by the presence of lateral inhomogeneities along the path of the beam and the effects of multiple Coulomb scattering (MCS) are poorly modelled by analytical methods. Knowledge of proton stopping powers only is not enough to correctly predict its effect through deterministic computation techniques. As emphasized by Paganetti, the use of Monte Carlo simulations can significantly increase the accuracy.

A second major contribution to the range uncertainty takes place in the conversion of the planning CT into proton RSP. Because the energy attenuation of protons along their trajectories is given by the stopping powers of the encountered tissues, a 3D map of the patient's RSP is required for treatment planning. Ideally, such an image should be obtained with proton computed tomography. Although an increasing number of groups worldwide are investigating 3D proton imaging, there exists no commercial system yet. Implementing a proton computed tomography system in a clinical environment remains a huge challenge. Therefore, the current approach to obtain a 3D RSP map of the patient relies on the conversion of an x-ray CT scan. Nevertheless, because there is no unique relationship between Hounsfield unit (HU) and RSP, their computations are tainted by uncertainties.

There exists several methods to perform this conversion. The stoichiometric calibration is widely accepted as the most accurate. To establish the conversion curve, both HU and RSP are computed based on mean atomic compostion of human tissues. Those data can be found in tables such as ICRU's [22], Woodard and White's [56], White *et al.* [54]. The curve is obtained by interpolating between the points corresponding to the tissues listed in those tables. As an example, the calibration curve obtained by Schneider *et al.* in their seminal paper [43] is shown in Fig. 1.6.

RSP may be computed through the approximated Bethe-Bloch formula [43]:

$$RSP = \rho_{e,t} \frac{\ln\left(2m_e c^2 \beta^2 / I_t (1-\beta^2)\right) - \beta^2}{\ln\left(2m_e c^2 \beta^2 / I_w (1-\beta^2)\right) - \beta^2} \tag{1.4}$$

where $\rho_{e,t}$ is the relative electron density of the tissue, m_e is the mass of the electron, β is the relative speed of the incident protons, I_t is the mean excitation energy of the tissue and I_w is the mean excitation energy of water. On the contrary, HUs depend on the CT scanner spectrum. Consequently, the relationship between HU and elemental compositions must be empirically established, for a specific device.

One of the main criticisms usually leveled about this method is the difference that may exist between elemental compositions found in tables and the actual compositions of the tissues of a specific individual. The content of human tissues is known to vary considerably between people being the same age [22]. Moreover, the composition of a given type of

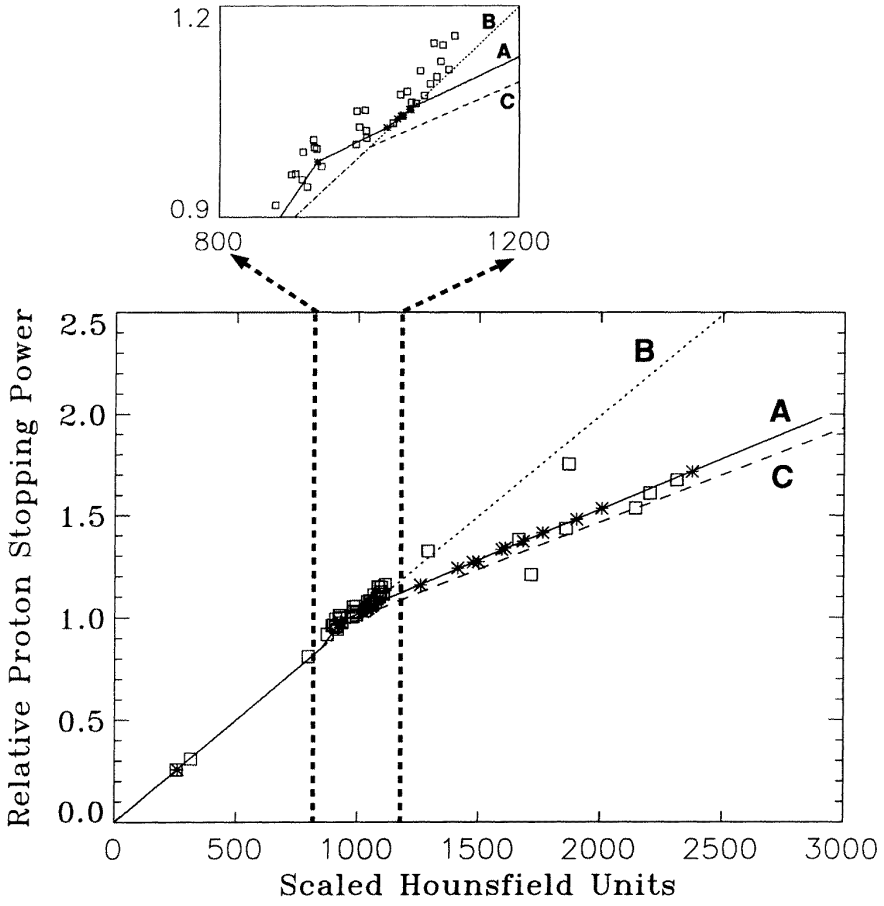

Figure 1.6: Calibration curves for the transformation of HU into RSP. The solid line shows the stoichiometric calibration (A) for biological tissues, the dotted and dashed lines show tissue substitute calibrations for two different types od tissue subsitutes (B and C). The squares represent calculations for tissue substitutes and the stars are calculations based on the chemical composition of real tissues. The small plot shows in detail the Hounsfield number range corresponding to soft tissue. From: [43].

tissue may depend on its location in the body.

Another major source of uncertainty taking place during the process

of establishing the conversion curve is related to the mean excitation energies of the tissues. Their values differ depending on the source [8, 23, 25]. Furthermore, the recommended value for the mean excitation energy of water has changed many times over the past decades [8, 23, 30, 38, 16, 5]. Any inconsistency between values used for water and tissues can contribute up to 3% to errors in RSP prediction [5, 37, 50].

1.3 *In vivo* range verification

1.3.1 Different techniques to reduce range uncertainty

Range uncertainty could be better understood, assessed and potentially corrected if *in vivo* range verification methods could be used. Unfortunately, there is still a remarkable lack of adequate techniques.

The most commonly used method is positron emission tomography (PET). It reconstructs an activation map of the tissues which have been irradiated by the protons. The quality of the results rapidly decreases over time which might be an issue when PET imaging has to be performed in a different room than the one used for treatment. An alternative method consists in imaging the gamma rays which are emitted during the excitation of tissues by the incident protons. A major advantage is that it is performed during treatment and does not require any additional in-room time. However, it has a much lower signal to noise ratio than direct measurements performed with a range probe, for instance. Experiments performed with a prototype of prompt gamma camera showed a 1 - 2 mm standard deviation in the range estimation inside homogeneous media [29].

1.3.2 Proton imaging

Despite their limitations, PET and prompt gamma imaging provide interesting perspectives in the context of adaptive proton therapy. Nonetheless, obtaining a 3D map of the RSP with proton computed tomography would directly solve the issue of the CT conversion. Furthermore, proton CT is not impacted by beam hardening which generates artifacts during an x-ray tomography reconstruction.

The use of protons for medical imaging applications was first suggested by Cormack more than fifty years ago in his seminal paper on

image reconstruction from line integrals [11]. Proton imaging has benefited from continuous developments since then. In 1981, a prototype of proton CT scanner was used at Los Alamos National Lab to image several objects including human organs [21]. Their experimental set-up is shown in Fig. 1.7. A multi-wire proportional chamber was used to measure the position of each proton at the exit of the phantom. A range telescope provided the residual energy. One of the drawbacks of such a system comes from the fact that protons undergo multiple Coulomb scattering (MCS) in objects. Hence, their paths and consequently their integral energy losses is a stochastic process which impacts CT reconstruction. Contemporary proton CT systems have a slightly different set-up, as shown in Fig. 1.8. It comprises two position trackers, one placed before and one after the phantom. The information provided by the two trackers can be used to estimate the most likely path of individual protons [44, 39].

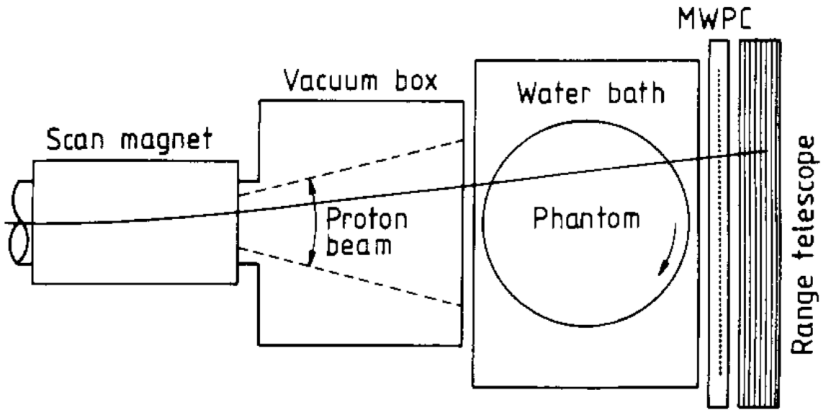

Figure 1.7: Schematic of an early proton CT scanner developed at the Los Alamos National Lab. A multi-wire proportional chamber and a range telescope were placed after the patient to measure individual proton histories. From [26].

In addition to the list-mode described above, proton imaging may be performed in the so-called integrated mode [41, 40]. Instead of tracking protons individually, their contributions are integrated. In pencil beam

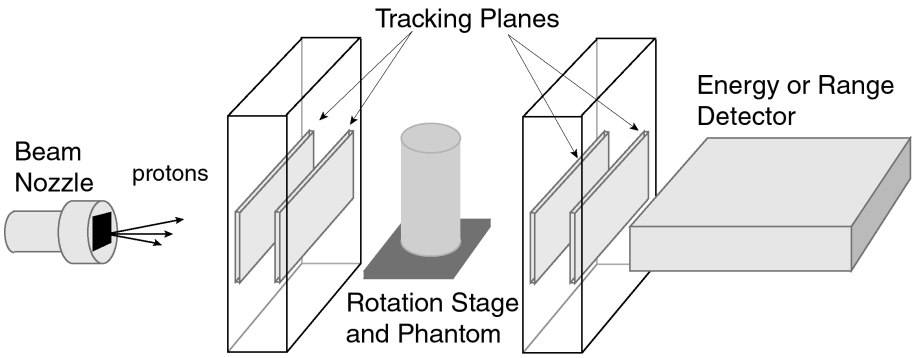

Figure 1.8: Schematic of a typical contemporary proton CT system. Position sensitive detectors are placed before and after the patient to track protons individually. From [21].

integrated mode proton radiography, the acquisition system is similar to the one presented in Fig. 1.8 but without the tracking planes. To deal with the lack of spatial resolution, proton beamlets are shot at known positions according to a regular grid of spots. Each spot correspond to a measurement performed by the detector. This decreases the overall complexity, cost and acquisition time of the system. However, this usually comes with higher dose delivered to the patient and lower image quality.

Despite the huge potential of proton CT to reduce range uncertainty and the continuous developments achieved in the field, no system can be considered as ready for clinical trials yet [26]. Moreover, the applicability of proton imaging is limited by the proton therapy system used in clinics. To achieve proton CT, the particles must traverse the patient in various directions. The energy of the protons must thus be significantly higher than those commonly used for treatment. Nevertheless, such high energies are rarely provided in most proton therapy facilities.

A correction of the CT conversion with a simple proton radiograph could appear satisfactory enough in most of the cases [49, 15]. Such optimization would be performed based on a map of range errors. This would be obtained by comparing measured ranges of high energy protons going through the patient with the ranges predicted based on the 3D map of the patient's estimated RSPs.

Proton radiography systems are fundamentally identical to those used for proton CT, except that there is no relative displacement of the acquisition device with respect to the phantom. Because of its simplicity and low cost, integrated mode proton radiography could rapidly be developed for a clinical usage. Paradoxically, it has been slightly forsaken during the last decade by research groups worldwide for the benefit of list-mode proton CT. The two last major developments were probably the energy resolved method [7] and the use of multi-layer ionization chambers (MLIC) [41, 19]. The energy resolved technique relies on a single layer detector. By varying the energy step by step, an energy-dose profile can be measured and the water equivalent thickness (WET) crossed by the protons can subsequently be inferred. On the contrary, with a multi-layer detector such as a MLIC, the WET may be directly determined from the measured dose deposition profile and from the knowledge of the incident energy. Some authors draw a distinction between WET and water equivalent path length (WEPL). In this thesis both names are used interchangeably.

Fig. 1.9 illustrates the principle of proton radiography using a MLIC. If protons have an initial energy large enough to traverse the patient, they eventually reach the detector. The integral dose deposition profile measured by the MLIC (measured IDD) is a shifted version of the one that would be measured without the patient through the beam path (reference IDD). Assuming that the detector was calibrated against water, this shift between the IDDs is equivalent to the WET of the patient. A radiograph is eventually obtained by performing such measurements on a regular grid of spots.

The use of a single energy for each spot is a great advantage from a dose perspective. Hence, the use of a MLIC for proton radiography presents all the advantages of integrated mode proton radiography while limiting the dose to be delivered to the patient. Moreover, commercially available devices, such as the Giraffe (IBA, Belgium), offer a sub-millimeter range accuracy. For these reasons, the use of a MLIC is the foundation of this thesis.

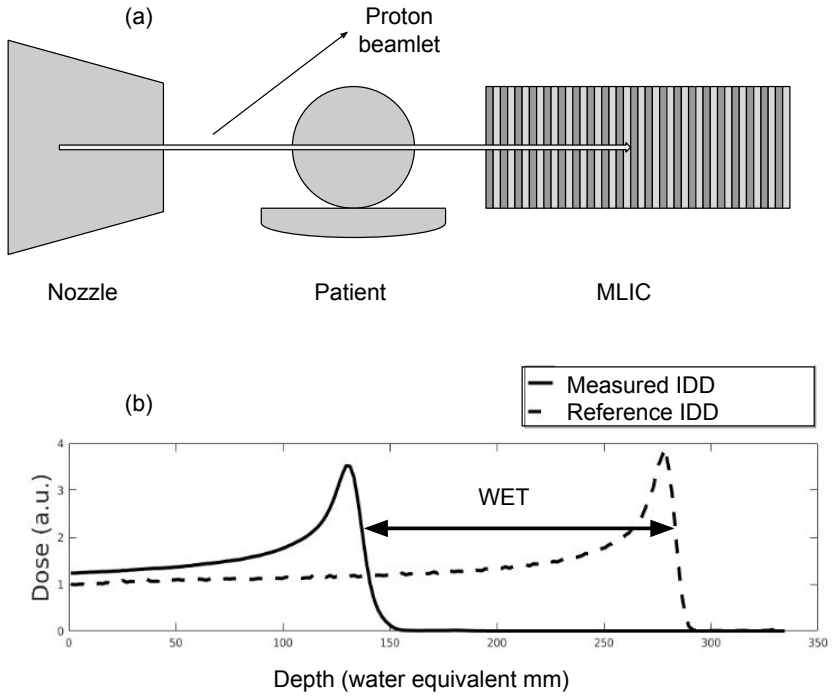

Figure 1.9: (a) Schematic of a proton imager relying on a MLIC. The WET of the patient may be directly determined based on the measured IDD and the reference one.

1.4 Aim and overview of the thesis

Proton imaging would certainly be the most direct way to quantify and reduce range uncertainty in proton therapy. In addition to yield quantitative information that are so far remarkably missing, it could also potentially be used to improve proton range estimation during treatment planning.

Since the use of protons for tomographic imaging was first suggested by Cormack in 1963 [11], many developments have been made with the aim of improving the estimation of RSPs for treatment planning. Despite those continuous developments in the field, no system is currently

used on patients although at least one private company - ProtonVDA Inc. - has engaged in bringing this technology in clinics [1]. However, several authors have shown that proton radiography could be satisfactory enough to quantify and potentially correct some of the contributions to range uncertainty [49, 15, 10]. In this thesis, we follow this last approach and aim at implementing a radiography technique that could achieve those objectives. To this end, we first conceive the acquisition process and demonstrate that it could measure range error in clinical conditions, ie. *in vivo*, and with a clinically acceptable accuracy. In addition, the possibility to reduce range uncertainty is also discussed in a more global context.

Particular emphasis is placed on designing a process that could be directly translatable in clinics. Therefore, we decide to focus on a simple and affordable technique which relies on a MLIC and which has benefited from some preliminary investigations carried out by Farace *et al.* [19]. The authors showed that the use of a MLIC was a promising solution both from a practical point of view and in term of performance. In this work, they compared measurements with simulations performed with their treatment planning system (TPS) to generate range error maps. However, some limitations should be addressed. First, a method independent on the use of a specific TPS would be desirable. In addition, the spatial resolution was pretty limited so as to maintain the delivered dose and the irradiation time relatively low. Particular attention should be paid to the fact that any increase in the spatial resolution should not be at the cost of this duration which must be sufficiently low, ie. within one minute, to mitigate the possibility of organ movements during the acquisition. Finally, range mixing which is caused by the presence of lateral inhomogeneities along the beam path is known to be a major issue in integrated mode proton radiography since it introduces some kind of 'blurring' in the data. The solution proposed by Farace *et al.* was to compare the measured data with simulations in which the range mixing was also modeled. But most analytic TPS poorly account for lateral inhomogeneities which may introduce large errors in range difference maps.

In this thesis, we push the technique further to have a complete system that first would not rely on a TPS. In addition, we develop methods to estimate more accurately range error maps without being impacted

by range mixing which is one of the biggest challenges of integrated mode proton radiography. To determine the required measurement accuracy, it must be taken into account that the range errors that we wish to measure are associated with an estimated uncertainty of about 3%. Moreover, the object to be imaged is considered to have of thickness of a few equivalent centimeters up to less that 33 equivalent centimeters since it is generally the maximum available range in clinical facilities. Therefore, we must be able to measure range errors ranging from one to several equivalent millimeters. Hence, a sub-millimeter accuracy is desirable. Finally, we implement post-processing methods to use larger spot spacings while having a spatial resolution of range error maps equivalent to the one of the planning CT.

At last, the main purposes of proton radiography as mentioned above are on the one hand to accurately quantify range uncertainty and on the other to offer a way to possibly correct it. Since RSPs are typically estimated based on a planning CT and a calibration curve, we investigate whether CT conversion could benefit from proton radiography to reduce errors in the estimated RSPs.

1.5 Thesis outline

This dissertation is conceived as a collection of chapters from published and sometimes not yet submitted articles so that a reader familiar with *in vivo* range verification could read them independently. Therefore, a few points are introduced redundantly in the different chapters.

In this thesis, we work at designing a proton radiography acquisition workflow that could easily be translated into clinical practice. The approach that we follow relies on the integrated mode acquisition method and more specifically on the use of a MLIC. It is a straight continuation of the pioneering study carried out by Farace *et al.* [19] which was briefly introduced in Section 1.3.2. If the simplicity of the system was highlighted as a major asset by the authors, it comes at the cost of limited spatial resolution and range accuracy. Therefore, a major part of this thesis focuses on elaborating post-processing methods aiming at producing range error maps with clinically acceptable characteristics.

We start by introducing, in Chapter 2, the acquisition technique which is based on the work of Farace *et al.* [19]. In a collaboration with

Ion Beam Applications (IBA, Belgium) and the authors, we fine-tune several parameters to make the technique acceptable for clinical trials. These include irradiation time as well as delivered dose. In addition, a module is implemented to load the data and permit future developments of post processing tools in openREGGUI, a Matlab based platform for adaptive proton therapy.

In Chapter 3, we develop a first method to generate range error maps in the context of CT conversion assessment. A fast and direct ray-tracing algorithm is implemented to simulate IDDs of which the comparison with data measured with a MLIC lead to an estimation of the range errors. The validity of the method is assessed with respect to the analytical and Monte Carlo dose engines of our treatment planning system. It outperforms analytical TPS and gives similar results compared to Monte Carlo with a considerably reduced computation time.

At this stage of the thesis, important limitations prevent any clinical workflow to be established as a straightforward implementation of the work presented in Chapter 2 and 3. First, the acquisition time is too high for common use in clinics mainly because of the limited entrance size of the commercial detector used in our preliminary studies. The duration to fully image a head phantom is approximately twenty minutes. However, it could be greatly decreased if a larger MLIC were available. To this end, a dedicated device is developed. With a field-of-view of 105×185 mm^2 proton radiographs of equivalent size could be acquired ten times faster. In order to limit production costs, a different type of electrode coating is proposed and tested in Chapter 4. Moreover, the study conducted in Chapter 3 shows a high sensitivity of range error maps to residual patient set-up errors. To mitigate the presence of this confounding factor in the context of CT conversion assessment, a specific registration method is developed in Chapter 5. The algorithm relies on the IDD simulation method developed in Chapter 3 and benefits from the information contained in the IDDs. In Chapter 6 we are able to experimentally show that it can correct set-up errors better than conventional kV-kV alignment.

Furthermore, we propose in Chapter 6 a method to better estimate and increase the spatial resolution of range error maps. Specifically, it relies on sparse optimization to estimate high resolution WET maps from low resolution proton radiographs. We show that the maps obtained

through the optimization have a submillimeter range accuracy which is acceptable for a clinical usage in the context of quality assurance.

Finally, in Chapter 7, we focus on the use of proton radiography to optimize the conversion curve from HU to RSP. A scientific critique of the state-of-the-art methods brings to light limitations that were not considered by the authors. Based upon these observations and some recent progresses in the field of treatment planning we discuss the relevance of the original idea to use proton radiography as a tool to improve CT conversion. We finally close this thesis by discussing more widely the scope of applications of proton radiography in the context of modern proton therapy.

Chapter 2

Pencil beam proton radiography using a commercial multi layer ionization chamber

The work in this chapter is based on a previous study carried out by Farace *et al.* [19]. It was presented at the following meetings:

- P Farace, R Righetto, S Deffet, F Vander Stappen, 2016. Pencil beam proton radiography using a multilayer ionization chamber, Proton therapy co-operative group (PTOCG) annual meeting, Prague, Czech Republic (Poster)
- S Deffet, P Farace, R Righetto, F Vander Stappen, 2016. Pencil beam proton radiography using a multilayer ionization chamber, IBA annual users meeting, Trento, Italy (Poster and software demo)

2.1 Introduction

Proton therapy has the potential to confine most of the dose to the target thanks to the physical property of protons called the Bragg peak. Unfortunately, range computation during treatment planning is tainted by

various uncertainties. To better ensure conformity of the dose delivered to the tumor and potentially reduce range uncertainty, it is necessary to acquire *in vivo* clinical data.

Among the various methods that could be used to perform *in vivo* range verification, proton radiography has the potential to achieve sub-millimeter accuracy. Although the feasibility of this concept has been investigated for more than fifty years [11], nowadays there is no commercial system available yet. Moreover, proton therapy has benefited, in the mean time, from the development of a second generation of treatment delivery technique based on the pencil beam scanning technology. Mumot *et al.* [34] proposed to take advantage of the capabilities of such a system to locally check the integrated stopping power with a range probe. Later, Rinaldi *et al.* [41] and Farace *et al.* [19] extended the concept to perform 2D radiography. In their study, Farace *et al.* presented a method to acquire pencil beam proton radiographs with a commercially available multi-layer ionization chamber (MLIC). The data measured by the device could then be compared with those predicted by their treatment planning system. This radiography technique forms the foundation of the studies presented throughout this thesis.

In collaboration with Ion Beam Applications (IBA, Belgium) and Paolo Farace and Roberto Righetto from the proton therapy center of Trento (APSS Trento, Italy) we settled measurements sessions to fine-tune several parameters in order to make the technique acceptable for preliminary clinical trials. These include irradiation time as well as dose delivered. Moreover, a plugin was implemented in the openREGGUI framework[1] to load and post-process the data.

In this chapter, we present the method imagined by Farace *et al.* with the slight improvements made during our stays at the proton therapy center of Trento.

[1]OpenREGGUI is a Matlab based open-source platform for adaptive proton therapy: https://openreggui.org/.

2.2 Materials and methods

2.2.1 MLIC

For our investigation of proton radiography using a MLIC, we used the same device that was considered by Farace *et al.* for their experimental study [19]. This detector, named Giraffe (IBA Dosimetry, Belgium), consists in a stack of 180 parallel plates ionization chambers as shown schematicaly in Fig. 2.1. The collecting plates are connected to a multi-channel electrometer of which the best achievable sampling time is 10 ms. The diameter of the MLIC entrance is 10 cm. However, the useful area at the entrance of the detector is only a 45 x 45 mm^2 square because of the angle formed by the beam and the center line of the detector. When a pencil beam of the highest energy available (230 MeV) is sent outside this square, the dose deposition at the Bragg peak may not be fully contained in the active area of electrodes located deeper in the MLIC.

Each chamber composing the MLIC has a depth of 1.8 mm equivalent to water. This value results from two parameters: the air gap between two electrodes (approximately 1 mm) and the thickness of each material present in the printed circuit board (PCB). The base material of the PCB shown schematically in Fig. 2.2 consists in DE156, a type of FR4 based on a modified epoxy resin. The collecting electrodes are made out of carbon which is closer to water than copper in term of density.

The output data of the MLIC were recorded in csv files with the OmniPro-Incline software (IBA Dosimetry, Belgium).

2.2.2 Acquisition set up

Proton radiographs were obtained by sending pencil beam shots having a high energy of 210 MeV capable of crossing the phantom later considered in this study. Each spot was spaced by 5 mm. As a result, each acquisition of a 45 x 45 mm^2 contained 81 spots. The beam irradiation was performed by the ProteusPlus (IBA, Belgium) of the APSS proton therapy center located in Trento, Italy, using 0.01 MU. The phantom was placed on the treatment couch and the MLIC was positioned at its exit side so as to measure the integral depth-dose profiles (IDD) of the protons after they crossed the phantom. A picture of the experimental set-up is shown in Fig. 2.3.

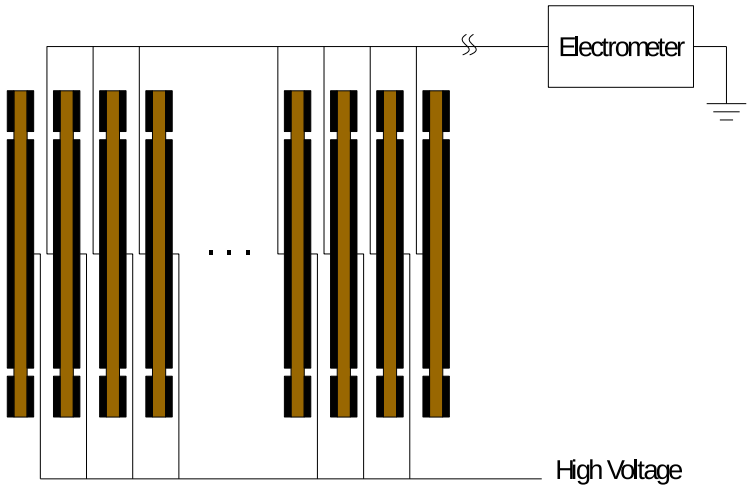

Figure 2.1: Schematic of the MLIC named Giraffe. It consists of 180 parallel plates separated by an air gap of approximately 1 mm. A bias voltage of 150V is applied between facing electrodes.

For our investigation of the use of the Giraffe for proton radiography, the anthropomorphic head phantom model 731-HN (CIRS, USA), was acquired in two directions corresponding to gantry angles of 270° and 0° so that the first radiograph was taken along the lateral direction and the second one along the antero-posterior direction.

To acquire a proton radiograph of the full area to be imaged, the couch supporting the phantom was moved to irradiate adjacent frames of size 45 x 45 mm^2, as shown in Fig. 2.4. For each frame, the data were recorded by OmniPro-Incline into a csv file. A program implemented in the openREGGUI framework was then used to read the data and to stick together all the frames.

In order to use the MLIC electrometer at its full potential (sampling time of 10 ms), the settling time of the proton therapy unit was increased to 30 ms. Such a value ensured that the electometer would measure a

Figure 2.2: Top view of an electrode - Image intentionally removed from the online version.

null signal after each pencil beam shots, allowing spot discrimination in post processing.

2.3 Results

2.3.1 Measurements

Proton radiographs are a collection of pairs consisting of the position of each one of the pencil beam shots and its corresponding measured IDD. This IDD is the integral on planes perpendicular to the beam direction of the dose deposition of each individual proton of the pencil beam shot.

The two orthogonal proton radiographs of the head phantom are shown in Fig. 2.5. At interfaces, the shape of the IDDs significantly differs from a pristine Bragg curve as a result of the transit of protons through lateral inhomogeneities. This phenomenon comes from the finite size of a proton pencil beam. When protons encounter lateral inhomogeneities, as illustrated in Fig. 2.6, the protons going through the dense tissues only will loose much more energy than the one going through the soft tissues. In addition, multiple Coulomb scattering may also contribute to the alteration of the measured curve.

The time required to move the couch between the acquisition of each frame composing the whole proton radiograph and to load the beams

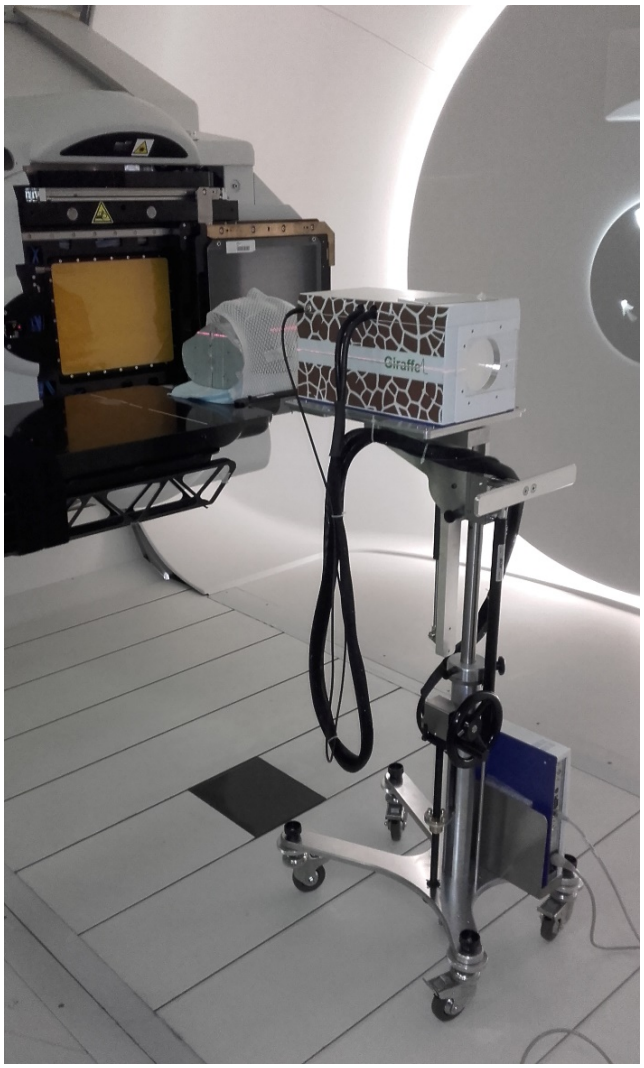

Figure 2.3: Experimental set up used for the acquisition of a proton radiograph of a head phantom along the lateral direction (gantry at 270°).

from the record and verify system was around 45 seconds. With a settling time of 30 ms, the time for acquiring a full proton radiograph such as the one of the head along the antero-posterior direction was approx-

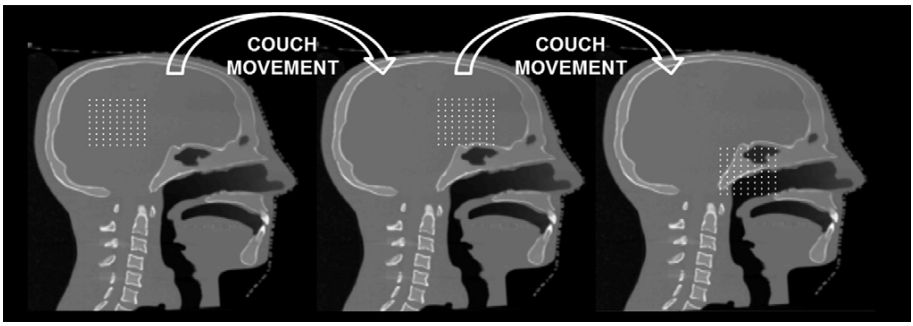

Figure 2.4: Acquisition of a full proton radiograph consists of multiple 45 x 45 mm^2 squares measurements interleaved by couch movements. Courtesy of Farace *et al.* [19].

imately 20 minutes, the irradiation time being negligible in comparison with the one spent in moving the couch.

2.3.2 openREGGUI

Two post-processing tools were implemented in the openREGGUI framework to process the data acquired with OmniPro-Incline. First, a loading interface takes charge of reading the data recorded in the csv files and stick them together in the right order based on some additional information encoded by the user. Secondly, a visualization tool allows to display a projection of a proton radiograph and the integral depth-dose profile associated with each pixel.

Fig. 2.7 shows a capture of the visualization interface. Several proton radiographs can be superimposed to simultaneously compare their underlying IDDs. To do so, a click on a pixel displays the corresponding data on the right panel.

2.4 Discussion

A method to obtain pencil beam proton radiographs with a MLIC was recently proposed [19]. In collaboration with IBA and the authors of this paper, we settled measurements sessions at the proton therapy center of Trento to fine-tune several parameters in order to make the tech-

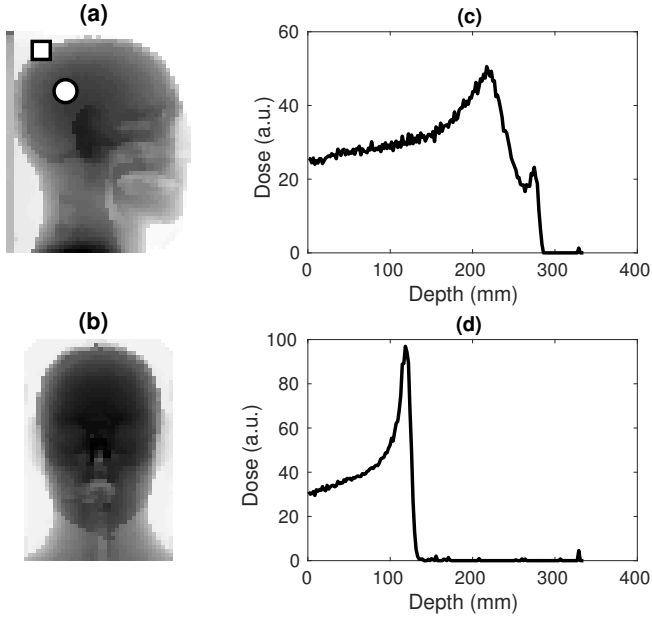

Figure 2.5: Projection in the form of range maps of the proton radiographs (a) obtained with a gantry angle of 270°and (b) with a gantry angle of 0°and examples of the IDD underlying each pixel such as (c) the one corresponding to the square dot and (d) the one corresponding to the round dot.

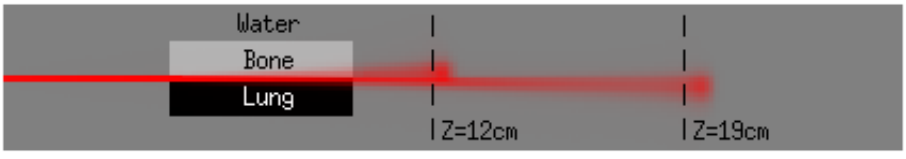

Figure 2.6: Monte Carlo simulation of the dose deposited by a 150 MeV proton pencil beam into a heterogeneous phantom composed of lung, water, and bone materials. From: [27].

nique acceptable for clinical trials. With the settling time presented in this study, a whole lateral proton radiograph of a head phantom was acquired in approximately 20 minutes, which can be considered feasible for

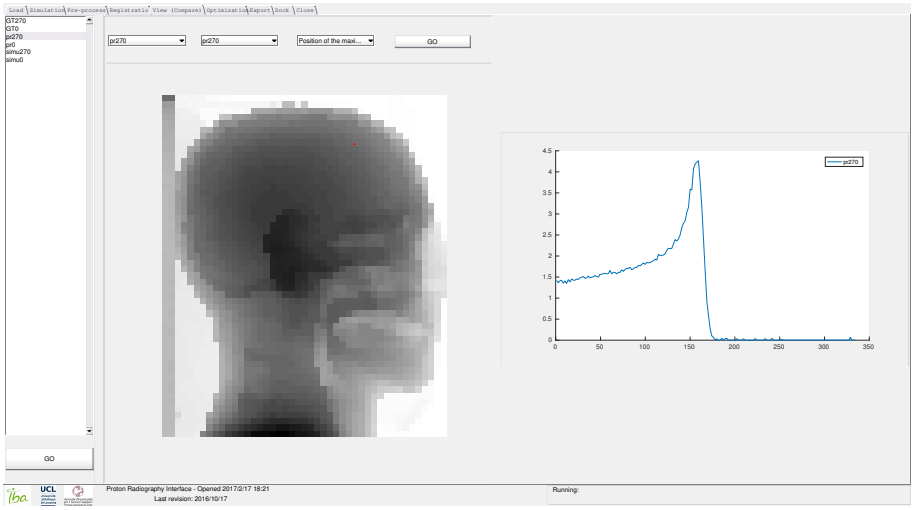

Figure 2.7: Capture of the proton radiograph visualization interface implemented in the openREGGUI framework. The Bragg curve displayed on the right panel corresponds to the pixel that was clicked on and which is marked by a red dot.

preliminary clinical trials. Most of the time needed to acquire a proton radiograph is now mainly spent in couch movements and in communications between the record and verify system and the treatment control system. Nevertheless, this acquisition time is too high for common use in clinics. It could be decreased by automatizing the actions manually performed to move the couch and prepare the beam or by considering the use of a larger MLIC.

Measured IDD were impacted by range mixing. This resulted from the finite size of the beam and the presence of lateral inhomogeneties in the beam path. In the proton therapy facility of Trento where our measurements were performed, proton beam was characterized by a bi-dimensional Gaussian cross section and a spot size of 3 mm (one sigma). Because of this range mixing, the integrated attenuation of the protons through the body cannot be directly determined. As an alternative for a quality analysis of the prescribed treatment and in particular, for seeking potential CT calibration errors, the measured data could be compared with simulations performed by the treatment planning system in order to

produce range error maps [19]. However, the potential sources of errors are not only CT calibration errors but they may also be modifications in the anatomy of the patient as well as set-up error during the proton radiography. In order to reduce the risk of anatomy deformation between the planning CT acquisition and the proton radiography, the present technique could be applied just after the acquisition of a CT.

In a previous study using a range probe for one-dimensional range verification, Mumot *et al.* [34] pointed out that range errors are sensitive to misalignment, particularly on areas presenting substantial lateral heterogeneities along the path of the beam. Because of this very high sensitivity, conventional kilovoltage alignment might not be sufficient and it could be necessary to develop a registration algorithm between proton radiographs and x-ray CT allowing correction of set-up errors in post-processing.

Finally, estimations performed with our treatment planning system showed that the dose delivered with such a method is less than 1cGyE which is comparable to the one delivered by megavoltage portal imaging [19].

2.5 Conclusions

This study presents a method that could be used for proton range measurements on patients with a sub-millimeter range accuracy. As proposed by other authors, the acquired data could be compared with simulations performed by the treatment planning system in order to produce range error maps. Both acquisition time and dose delivered to the patient are acceptable for preliminary clinical trials. Nevertheless, the acquisition time should be decreased before the method could be used in clinical routine.

Chapter 3

A direct ray-tracing method to compute integral depth dose in pencil beam proton radiography with a multilayer ionization chamber

This chapter was written in the context of a collaborative work between UCLouvain, IBA and APSS Trento. It is a slightly adapted version of the paper mostly written by Paolo Farace [18] in which we have taken part in the data acquisition, the implementation of the data processing tools and the results analysis.

This work was presented in the following journal article and at the following meetings:

- P Farace, R Righetto, S Deffet, A, Meijers, F Vander Stappen, 2016. A direct ray-tracing method to compute integral depth dose in pencil beam proton radiography with a multilayer ionization chamber, Medical physics 2016 43 (12), 6405-6412

- S Deffet, P Farace, R Righetto, F Vander Stappen, 2016. Pen-

cil beam proton radiography using a multilayer ionization chamber, IBA annual users meeting, Trento, Italy (Poster and software demo)

- S Deffet, P Farace, R Righetto, B Macq, F Vander Stappen, 2017. SU-G-TeP2-13: Patient-Specific Reduction of Range Uncertainties in Proton Therapy by Proton Radiography with a Multi-Layer Ionization Chamber, Fifty-eighth annual meeting of the american association of physicists in medicine, Washington DC, USA (Poster)

The full text of this chapter may be found in
P Farace, R Righetto, S Deffet, A, Meijers, F Vander Stappen, 2016. A direct ray-tracing method to compute integral depth dose in pencil beam proton radiography with a multilayer ionization chamber, Medical physics 2016 43 (12), 6405-6412

Chapter 4

Design and implementation of a MLIC dedicated to proton radiography

4.1 Introduction

Proton radiography based on multi-layer ionization chamber (MLIC) has benefited from a recent body of research which demonstrated its potential to better quantify and potentially reduce the range uncertainty [41, 19]. In Chapter 2, we presented an acquisition method first developed by Farace *et al.* [19] for a commercially available device, the Giraffe (IBA, Belgium). Radiographs were obtained by scanning through a phantom and recording the pairs consisting of the position of each of the pencil beam shots and its corresponding measured integral depth-dose (IDD) profile.

With a sub-millimeter range accuracy and a dose received by the patient comparable to the one delivered by mega-voltage portal imaging, MLIC appeared to be a promising tool for proton radiography. Nonetheless, the acquisition time (twenty minutes) could limit clinical applications. This long duration was the result of the relatively small field of view (45 x 45 mm^2) and of the couch movements required to image the full area. To establish the full potential of proton radiography using a MLIC, we need to assess the feasibility of a large field-of-view device. In this chapter, we develop such a detector. In the first instance, techni-

cal choices and main characteristics are detailed. In particular, to limit production costs, we propose to use standard copper over FR4 for the electrodes. The suitability of the materials are then assessed via Monte-Carlo simulations. Finally, some preliminary measurements performed with a prototype are presented.

4.2 Materials and methods

4.2.1 Design and implementation

Multi-layer ionization chamber

The MLIC consists in a series of electrodes with an active area of 160 x 260 mm^2 and which are separated by 1.3 mm of air. The area was limited so as to keep a weight such that manual use and transportation would be possible. It was estimated to 16 kg, without housing. Assuming that the lateral scattering caused by the protons crossing the electrodes is negligible, such a surface should result in a field of view (projected on the isocenter plane) of 133 x 223 mm^2 (computed for a source - axis distance (SAD) of two meters, a detector placed at thirty centimeters from the isocenter, and a spot size of 5.9 millimeter at 1.96σ).

The collecting side of an electrode is shown in Fig. 4.1[1]. As opposed to the Giraffe, it exhibits a rectangle area which is more suitable for scanning than a circular one. A guard ring encircles the tracks and the areas conveying signals, wherever it is possible. The printed circuit board (PCB) has only two layers to achieve a uniform thickness.

The core material of the electrodes is a standard FR4 substrate of thickness 1.2 mm. Copper thickness is 35 μm. An electroless nickel immersion gold (ENIG) surface finish was chosen for its planarity, small thickness and high shelf life. It is a two layer metallic coating of approximately 1 μm gold over 3 μm nickel[2]. As a result, the water equivalent thickness (WET) of an electrode was estimated to be approximately 2.5 mm. Consequently, 128 of those were required to cover 320 mm which is the range in water of 226 MeV protons.

Electrodes were imbricated into two PCBs of which the drawings may be found in appendix B: a base plate and a top plate. The aim of the

[1] More technical drawings may be found in appendix B.

[2] Surface finish thickness may vary from one manufacturer to another.

Figure 4.1: Electrode (collecting side) - Image intentionally removed from the online version.

base plate is to convey signals and voltages whereas the top plate only plays a mechanical role. As for electrodes, signal tracks on those PCBs were protected from leakage current by guard rings. The connectors (DB37) are identical to those of the electrometer detailed below. High voltage is brought via a coaxial cable and is shared by all the electrodes. Hence, electrometers must all have the same reference.

The final assembly in a housing made out of laser-cut acrylic glass is shown in Fig. 4.2. A shielding in aluminum sheets was later added.

Electrometer

The electrometers used in this study were primarily designed by Dekimo (Germany) to measure ionization currents in the ionization chambers of IBA nozzles. The system is based on DDC316 chips from Texas Instruments which are 16-channel current-input analog-to-digital converters. Each electrometer has four of these chips so that two devices are required for our 128 electrodes MLIC. The provided resolution after internal processing is 1 bit / 3 fC yet the minimal readable current is only specified as lower than 10 pA. The internal sampling frequency is 50 kHz. Channel offsets and gains are configurable. The gain calibration is a factory setting that can be updated anytime with a specific hardware. Offset compensation depends on the environment and should be recalculated

Figure 4.2: Final assembly in a housing made out of laser-cut acrylic glass - Image intentionally removed from the online version.

before any measurement.

4.2.2 Experimental characterization

Monte-Carlo simulations

The composition of the electrodes is detailed in Table 4.1. Material thicknesses were provided by the manufacturers (Kapi s.a., Belgium - PCBWay, China - Eurocircuits, Belgium). FR4 composition may vary between manufacturers and could not be precisely determined. A mix of 60% glass fiber (E-glass) and 40% epoxy resin (Epotek 301-1) was used in the simulations.

The use of materials of relatively high atomic number ($Z_{Ni} = 28$, $Z_{Cu} = 29$, $Z_{Au} = 79$) and density might lead to differences in multiple Coulomb scattering (MCS) and energy straggling. This can not only impact expected signals but also the field of view. To assess their effects, Geant4 simulations were conducted via GATE. The reference physics list QuarkGluonStringG4Precompound – BInaryCascade – HighPrecision neutron (QGSP-BIC-HP) was used with the SingleScattering process enabled instead of the MultipleScattering.

For each simulation performed in this study, the entrance of the detector was placed at 30 cm from the isocenter, the exit of the nozzle was at 50 cm from the isocenter and the SAD was 2 m. The spot size

Volume No	Material	Thickness (mm)	Density	Composition (mass fractions)
1	Gold	0.001	19.3	$w_{Au} = 1$
2	Nickel	0.003	8.91	$w_{Ni} = 1$
3	Copper	0.035	8.96	$w_{Cu} = 1$
4	FR4	1.2	1.9	$w_{Si} = 0.15$
				$w_{O} = 0.36$
				$w_{Ca} = 0.08$
				$w_{Al} = 0.04$
				$w_{Mg} = 0.01$
				$w_{B} = 0.01$
				$w_{K} = 0.01$
				$w_{C} = 0.27$
				$w_{H} = 0.03$
				$w_{N} = 0.03$
				$w_{Na} = 0.01$
5	Copper	0.035	8.96	$w_{Cu} = 1$
6	Nickel	0.003	8.91	$w_{Ni} = 1$
7	Gold	0.001	19.3	$w_{Au} = 1$
8	Air	1.3	$1.29\ 10^{-6}$	$w_{N} = 0.76$
				$w_{O} = 0.23$
				$w_{Ar} = 0.01$

Table 4.1: Electrodes elemental composition.

was 3 mm (one sigma at 100 MeV). The initial energy of the incident protons was 210 MeV.

In the first instance, the difference of impacts between the cumulated thickness of metals and an equivalent thickness of water is studied. In the MLIC, the cumulated thicknesses, T, are: $T_{Cu} = 8.96$ mm, $T_{Ni} = 0.76$ mm, $T_{Au} = 0.256$ mm. These three volumes were placed at the isocenter and the dose was recorded in a water tank positioned at their exit side, in the path of the beam. A similar simulation was then performed with an equivalent thickness of water in place of the metals. This water equivalent thickness, named WET_m, would be determined by computing the shift between the IDD simulated with the volumes of metals, named IDD_m, and the one obtained after removing them,

named IDD_{air}:

$$WET_m = \arg\min_s \sum_{i=1}^{N} \left(IDD_{air}(z_i + s) - IDD_m(z_i)\right)^2 \tag{4.1}$$

Secondly, the use of FR4 was also investigated. The same experimental plan as detailed above for metals was used. The FR4 cumulated thickness is 153.6 mm. For the experiment, only 120 mm were considered so as to have a Bragg peak fully contained in the water tank.

Thirdly, the MLIC was fully modelled as a series of volumes which were repeated 128 times. Their characteristics were those listed in Table 4.1. An actor was attached to each volume of air to record the integrated dose. Two experiments were done: one without any object through the beam path and one with a volume of water (thickness $T_w = 150$ mm). The WET of the electrodes would be estimated by computing the shift between the IDD simulated with no object through the beam path, named IDD_{air}, and the one obtained with the water tank placed at the isocenter, named IDD_w:

$$WET = \frac{T_w}{\arg\min_s \sum_{i=1}^{N} \left(IDD_{air}(z_i + s) - IDD_w(z_i)\right)^2} \tag{4.2}$$

Finally, the field of view was investigated by scanning through the detector with a spot spacing of 5 mm and an initial energy of 210 MeV.

Measurements

Some preliminary measurements were performed at the proton therapy facility of Essen (Germany) with a prototype corresponding to the 3D drawing shown in Fig. 4.2. For this first measurement session, the MLIC was only populated with 36 electrodes. A volume of solid water (thickness 2.5 inch.) was added at the entrance of the device. The beam was operated in continuous mode and the energy was varied. Corresponding ranges in water were 8.72 cm, 9.72 cm, 10.72 cm, 11.72 cm, 12.72 cm, 13.72 cm, and 14.72 cm. For each energy, an IDD was measured with an integration period of 20 ms.

4.3 Results

4.3.1 Monte-Carlo simulations

Fig. 4.3 shows the experimental set-up implemented in GATE on the left panel and the IDD simulated with an initial energy of 210 MeV on the right panel. In this first study, a water tank was placed instead of the detector so as not to introduce additional sources of perturbation. The aim was to study the impact of 8.96 mm of copper, 0.77 mm of nickel and 0.26 mm of gold on the dose profiles. Two curves are shown. A first one was obtained without any object in the beam path. The second curve was acquired after adding the cumulated volumes of metals between the nozzle and the MLIC. The shift between the IDD is 61 mm.

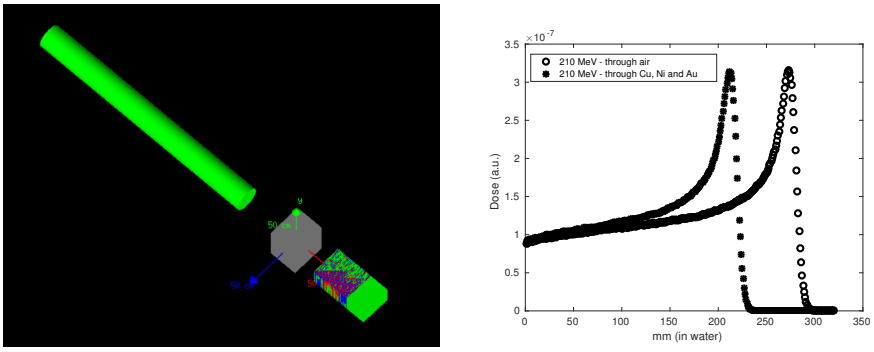

(a) (b)

Figure 4.3: (a) Experimental set-up implemented in GATE. The beamline is simply modelled as a vacuum tube. Depending on the experiment a volume (shown in gray on the figure) may be present in the beam path and the MLIC may be fully modelled or replaced by a water tank. (b) IDDs simulated with and without metals (9mm Cu, 0.77 Ni and 0.26 mm Au) through the beam path.

In Fig. 4.4, a similar simulation performed with 61 mm of water placed at the isocenter is compared with the previous case. Moreover, 2D dose maps were recorded at a depth of 50 mm in the water tank. The IDD in both cases perfectly coincide but the dose maps significantly differ. An increase of the spot size related to a higher scattering is clearly visible when protons go through the volumes of metals. Fortunately, this

did not have an impact on the shape of the IDD. Although the size of the beam increased because of the presence of metals, the integrated dose delivered in planes perpendicular to the beam remained fairly identical.

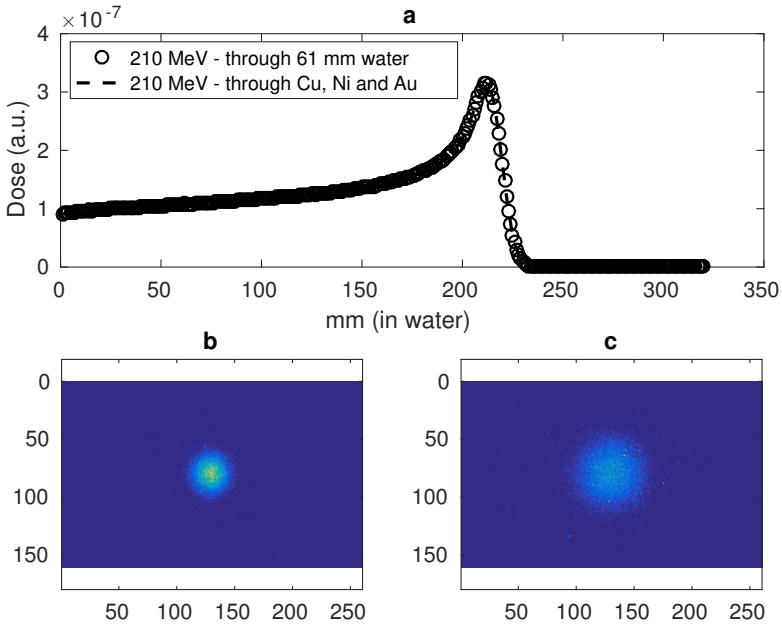

Figure 4.4: (a) IDDs simulated in a water tank (resolution 1mm) after protons traversed 61 mm of water and 8.96 mm of copper, 0.76 mm of nickel and 0.256 mm of gold. (b) 2D dose map at a depth of 50 mm in the water tank after protons traversed 61 mm of water and (c) after they traversed 8.96 mm of copper, 0.76 mm of nickel and 0.256 mm of gold.

A similar experiment was reproduced for FR4. A volume having a thickness of 120 mm was placed at the isocenter and the IDD simulated in the water tank was compared with the one obtained with an equivalent thickness of water. Results are shown in Fig. 4.5. Again, the IDDs perfectly coincide. MCS appears to be similar in both cases but interestingly the IDD obtained in the case of water shows a slightly higher energy straggling.

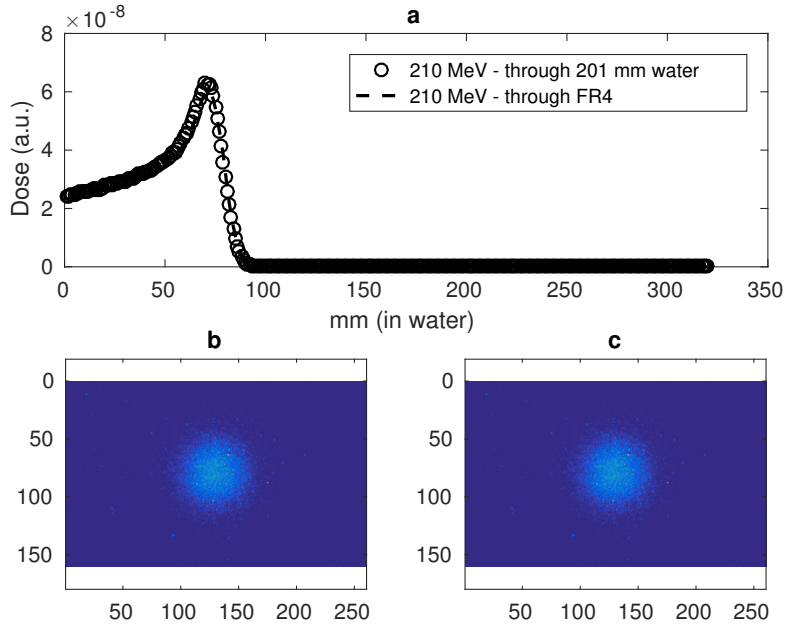

Figure 4.5: (a) IDDs simulated in a water tank (resolution 1mm) after protons traversed 201 mm of water and 120 mm of FR4. (b) 2D dose map at a depth of 50 mm in the water tank after protons traversed 201 mm of water and (c) after they traversed 120 mm of FR4.

Fig. 4.6 shows IDDs simulated with the detector fully modelled. Two simulations were performed: one with a water box (thickness 150 mm) placed at the isocenter and one without any object through the beam path. The corresponding IDDs are named IDD_{water}^{MLIC} and IDD_{air}^{MLIC}. On the right panel, IDD_{air}^{MLIC} was shifted so as to match IDD_{water}^{MLIC} in term of squared difference. Their coincidence is almost perfect, which demonstrates that the difference in energy straggling is tiny and that there is no signal degradation caused by MCS. Using Eq. 4.2, we found that the WET of each electrode was 2.45 mm.

Finally, four simulations were performed to assess the field of view of the device. Fig. 4.7 shows IDDs simulated on a horizontal line of spots spaced by 5 mm with an energy of 210 MeV. Position $X = 0$ corresponds

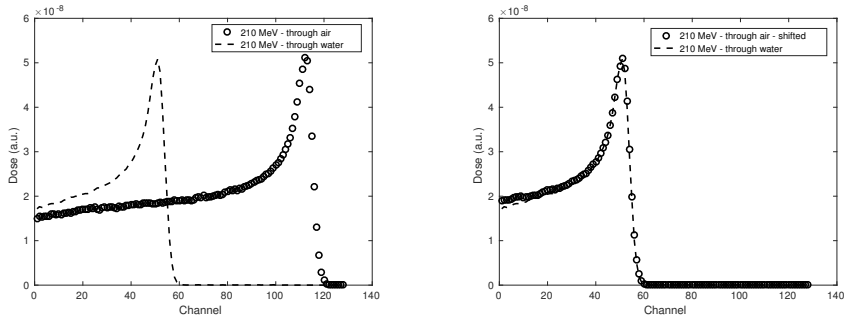

(a) (b)

Figure 4.6: (a) IDDs obtained by simulating all layers of the MLIC. Two curves are shown: one obtained with 150 mm of water placed at the isocenter and one without any object through the beam path (b) The IDD simulated through air was aligned with the one obtained with the volume of water in the beam path.

to the isocenter. Fig. 4.8 shows a similar experiment with a vertical line of spots. The IDDs appear to be degraded after $X = 52.5$ mm on the horizontal axis and $Y = 92.5$ mm on the vertical axis. To check that IDDs are not further degraded at the corners of the electrode, two similar experiments were performed with a horizontal line of spots at $Y = 92.5$ mm and a vertical line at $X = 52.5$ mm but are not graphically presented here. They confirmed a field of view of $105 \times 185\text{mm}^2$.

4.3.2 Measurements

Fig. 4.9 shows some preliminary measurements for various energies performed with a prototype populated with only 36 electrodes.

The WET of an electrode is 2.5 mm which is in agreement with both Monte Carlo simulations and theoretical expectations formulated in Section 4.2.1.

4.4 Discussion

Recent works have demonstrated the potential of MLIC to acquire proton radiographs. In 2016, Farace *et al.* proposed an acquisition tech-

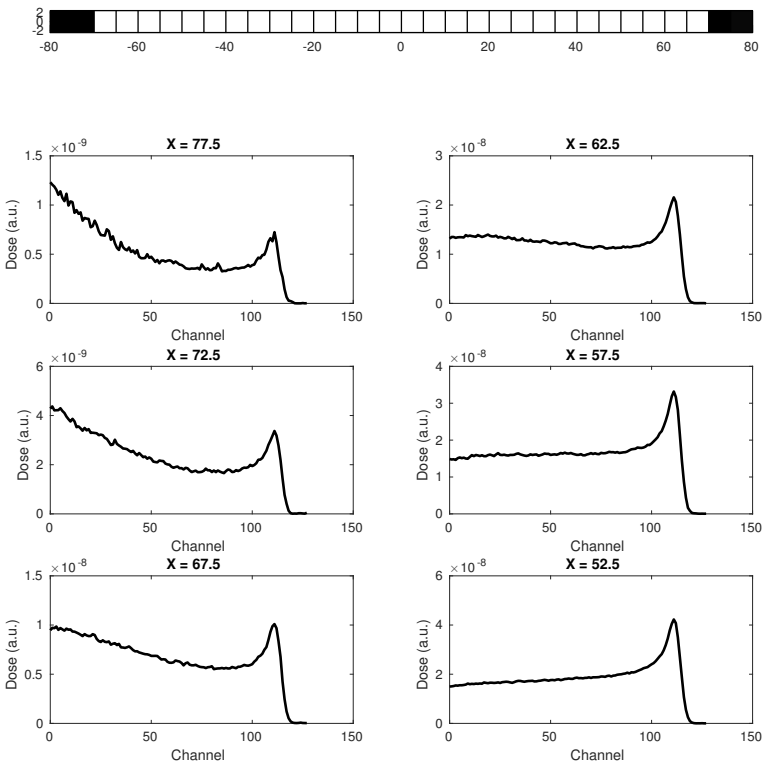

Figure 4.7: IDDs simulated in the MLIC fully modelled, for a horizontal line of spots spaced by 5 mm. Initial energy was 210 MeV.

nique relying on the Giraffe (IBA, Belgium) [19]. A set of dedicated tools were then developed to assess range uncertainty of which a major part comes from the conversion from the CT into RSP [18, 12, 13]. Image quality and dose delivered to the patient were considered acceptable for clinical use [19, 18]. Nevertheless, this radiography technique would benefit from a decrease in the acquisition time which was twenty minutes

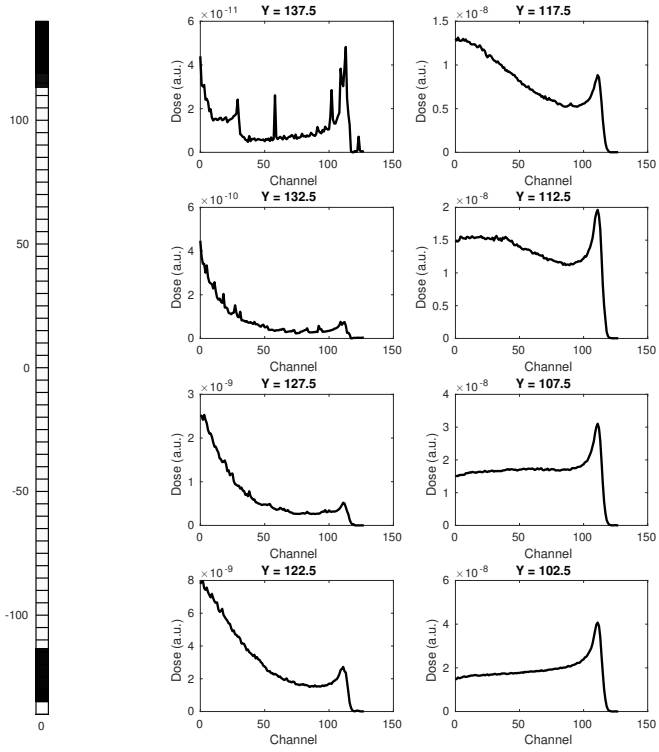

Figure 4.8: IDDs simulated in the MLIC fully modelled, for a vertical line of spots spaced by 5 mm. Initial energy was 210 MeV.

to fully image a head phantom. Most of the time was spent in couch movements.

In this chapter, we have studied the feasibility of a MLIC having a sensing area of 160×260 mm^2. Monte Carlo simulations showed that the field of view (projected on the isocenter plane) should be around 105×185 mm^2 for a SAD of 2 m, a detector placed at 30 cm from the isocenter, and a spot size of 3 mm (one sigma). Consequently, a proton radiograph of 210×185 mm^2 could be acquired with only one couch movement and so in approximately one minute. This field of view

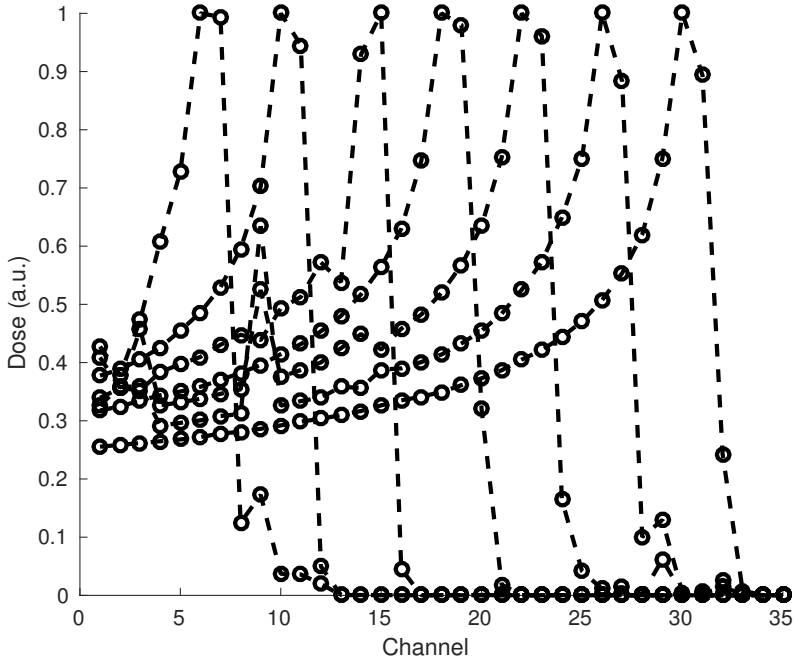

Figure 4.9: Measurement performed with a prototype MLIC. Corresponding ranges in water are 8.72 cm, 9.72 cm, 10.72 cm, 11.72 cm, 12.72 cm, 13.72 cm, and 14.72 cm. A volume of solid water (thickness 2.5 inch.) was placed in front of the device.

is actually smaller than the one theoretically expected in Section 4.2.1. This probably results from MCS of which the importance is increased by the presence of metals (copper, nickel and gold) in the electrodes. This is actually a major difference with respect to the Giraffe of which the electrodes are coated with carbon. Nevertheless, we demonstrated via Monte Carlo simulations that the IDDs were not impacted by the presence of metals.

Another difference with respect to the Giraffe is the WET of the electrodes which is 35% larger in our design. There is currently a lack of studies on the optimal sampling of IDDs in the context of proton radiography. This is however a paramount information that should be

discussed in regards to the processing methods that have been developed to assess range uncertainty with proton radiography using a MLIC. Obviously, the PCB thicknesses could be chosen smaller if necessary.

An incomplete prototype was tested during a short night shift at the proton facility of Essen (Germany). Although limited, the results shown in Fig. 4.9 are promising. The WET of the electrodes correspond to the ones estimated from the assumed compositions listed in Table 4.1. Regarding future perspective, the MLIC should be fully characterized through measurements in order to confirm the results of the Monte Carlo simulations and before acquiring the first proton radiographs. The signal to noise ratio should also be studied with respect to the dose since this parameter is paramount in medical imaging.

4.5 Conclusions

Throughout this thesis, we consider a commercially available MLIC, the Giraffe (IBA, Belgium), to perform proton radiography. Nonetheless, our method could benefit from a decrease in the acquisition time. To this end, a prototype of a MLIC with a larger field of view is being developed. In this study, we demonstrated via Monte Carlo simulations that standard copper over FR4 PCB could be used for the electrodes, with adequate surface finish. The field of view of the device is expected to be 105×185 mm^2 which is more than nine times the one of the Giraffe.

Chapter 5

Registration of proton radiography data with x-ray CT

The work in this chapter was presented in the following journal article and at the following meeting:

- S Deffet, B Macq, R Righetto, F Vander Stappen, P Farace, 2017. Registration of Pencil Beam Proton Radiography Data With X-Ray CT. Medical physics 2017 44(10) 5393–5401 (Research article)
- S Deffet, P Farace, F Vander Stappen, B Macq, 2018. Innovative Post-Processing Methods For Proton Radiography Data. Belgian Hospital Physicists Association (BHPA) annual meeting, Charleroi, Belgium (Oral)

The full text of this chapter may be found in
S Deffet, B Macq, R Righetto, F Vander Stappen, P Farace. Registration of Pencil Beam Proton Radiography Data With X-Ray CT. Medical physics 2017 44(10) 5393–5401

Chapter 6

Water equivalent thickness estimation via sparse deconvolution of proton radiography data

The work in this chapter was presented at the following meetings:

- S Deffet, P Farace, F Vander Stappen, B Macq. 2017, Status of the development of a proton imaging system, Réunion du GdR ISIS: Co-conception : capteurs hybrides *et al.*gorithmes pour des systèmes innovants, Paris, France (Poster)

- S Deffet, B Macq, F Vander Stappen, P Farace, 2018. Water Equivalent Thickness Estimation via Sparse Deconvolution of Proton Radiography Data. IEEE International Conference on Acoustics, Speech and Signal Processing, Calgary, Canada (Oral)

6.1 Introduction

During the last decade, two main types of proton radiography systems emerged. On the one hand, the so-called list-mode proton radiography relies on proton trackers placed before and after the patient and on a detector that can measure the residual energy. By tracking protons

individually, their trajectories inside the patient may be estimated and linked to their measured energy loss. On the other hand, in the so-called integrated mode proton radiography, the contributions of every protons are summed up. This decreases the overall complexity of the system of which the main limitations are the high data acquisition rate of the electronics and costs. Reciprocally, the main limitation of the integrated mode is the degradation of the signal caused by the presence of lateral inhomogeneties along the path of the beam and, to a lesser extent, by multiple Coulomb scattering (MCS).

Recently, the use of multilayer ionization chambers (MLIC) has benefited from a body of research which demonstrated its clinical potential [41, 19]. The radiography were performed with pencil scanning by delivering a set of beamlets uniformly spaced. An integral depth dose (IDD) profile was measured for each spot by the detector placed at the exit side of the patient. Because the shape of IDDs are impacted by the transit of protons through lateral inhomogeneties in a process called range mixing, one can not directly determine the integrated relative proton stopping power, also referred to as water equivalent thickness (WET), from the measurements. Two approaches currently exist. On the one hand, Farace *et al.* [19] implemented the idea proposed by Mumot *et al.* [34] of performing a comparison between the IDDs measured by the MLIC with those simulated by a treatment planning system. On the other hand, Krah *et al.* [28] proposed to decompose each IDD into a set of pristine Bragg curves from which the WET would be directly obtained. To spatially distribute the WET determined by the decomposition, the use of a WET map estimated from the planning CT was shown to improve greatly the results of a demosaicing step based on the radiography data only.

However, one can be concerned by the robustness of such a two-step method. In proton therapy, pencil beams exhibit a bi-dimensional Gaussian cross sectional profile. The WET estimation problem is consequently particularly ill-posed and the solution might be strongly affected by measurement noise. Moreover, the use of the planning CT in the two methods makes them sensitive to errors in the relative proton stopping power (RSP) computation and to residual set-up errors. The WET map estimate could also be altered by changes in the anatomy of the patient and relative displacements of moving organs that could take place

between the CT acquisition and the proton radiography.

In this chapter, we show that under the assumption that the WET map has a sparse representation, it can be obtained without using any prior knowledge derived from the planning CT. An iterative algorithm is built to perform a deconvolution of the IDDs and to increase the spatial resolution of the WET map. We then propose to combine planning CTs and proton radiographs, in a robust fashion, to further increase the deconvolution accuracy. The two methods are applied to both synthetic data and actual proton radiography acquisitions.

6.2 Materials and methods

6.2.1 Deconvolution

As experimentally demonstrated by Farace *et al.* [18] the measured IDDs, named IDD_m consists of a convolution of a Gaussian kernel G having a standard deviation equal to the spot size with shifted versions of a pristine Bragg curve, called IDD_{ref}, which corresponds to the IDD that would be measured without the phantom through the beam path:

$$\begin{aligned} IDD_m(x_i, y_i, z) \quad &\approx \quad \sum_{j \in S_i} G(x_i - x_j, y_i - y_j) \\ &\qquad IDD_{ref}(z + W(x_j, y_j)) \end{aligned} \tag{6.1}$$

where (x_i, y_i) are the coordinates of each pencil beam, z refers to the depth axis of the IDD, W refers to the water equivalent thickness of the phantom along the path of the beam and S_i denotes the set of the indices of the pixels lying in the cross-section of the beamlet. In the case of parallel beamlets, the WET can be estimated from the Hounsfield units (HU) of the planning CT via

$$W(x, y) = \sum_z RSP(HU(x, y, z)) s_z \tag{6.2}$$

where RSP is usually a piecewise linear function associating to each HU the RSP, and s_z is the size of a voxel along the z-direction.

In the absence of any other information than the proton radiograph, the WET estimation could be expressed in the form of an optimization

problem:

$$\begin{aligned} W^{opt}(x,y) &= \arg\min_{W} \sum_x \sum_y \int_0^{l_d} (IDD_m(x,y,z) \\ &\quad -D\left(\left(\ G(x,y)\right.\right. \\ &\quad \left.\left.\star IDD_r(z+W(x,y))\right)\right)^2 dz \end{aligned} \tag{6.3}$$

where D is the down-sampling function associated with the spot spacing and l_d is the depth of the detector.

Because of the down-sampling and the convolution with a Gaussian kernel, this problem is ill-posed.

For clarity, we now consider a matrix formulation of the equations. In this matrix format, Eq. 6.1 becomes:

$$\boldsymbol{IDD_m}(z) \approx \boldsymbol{G}\ \boldsymbol{IDD_r}(z\mathbb{1} + \boldsymbol{W}) \tag{6.4}$$

where $\boldsymbol{G}$ is the circulant matrix associated with the convolution kernel G and $\boldsymbol{IDD_r}$ is defined by

$$IDD_{r,i}(z) = IDD_{ref}(z) \tag{6.5}$$

We consider a transform $\boldsymbol{\Psi}$ such that the WET can be represented through the coefficients $\boldsymbol{\alpha}$:

$$\boldsymbol{W} = \boldsymbol{\Psi\alpha} \tag{6.6}$$

In this study, $\boldsymbol{\Psi}$ is the matrix associated with an inverse wavelet transform.

Under sparsity assumptions, one could recover the WET by solving the problem

$$\begin{aligned} \boldsymbol{\alpha^{opt}} &= \arg\min_{\boldsymbol{\alpha}} ||\boldsymbol{\alpha}||_0 \\ &\text{s.t.} \quad f_1(\boldsymbol{\alpha}) \leq \epsilon \end{aligned} \tag{6.7}$$

where the function $f_1(\boldsymbol{\alpha})$ is a similarity measure (already introduced in Eq. 6.3) between the measured data and the model consisting of Eq. 6.4 and 6.6:

$$\begin{aligned} f_1(\boldsymbol{\alpha}) = \int_0^{l_d} & ||\boldsymbol{IDD_m}(z) \\ & -\boldsymbol{G}\ \boldsymbol{IDD_r}(z\mathbb{1} + \boldsymbol{\Psi\alpha})||_2^2\, dz \end{aligned} \tag{6.8}$$

Relaxing Eq. 6.7 with a l_1 norm and assuming that f_1 is convex, the minimization problem can be solved with the proximal method which provides an iterative algorithm:

$$\boldsymbol{\alpha_{n+1}} = \text{prox}_{\gamma, f_2}\left(\boldsymbol{\alpha_n} - \gamma \nabla f_1(\boldsymbol{\alpha_n})\right) \tag{6.9}$$

with

$$f_2(\lambda, \boldsymbol{\alpha}) = \frac{1}{2\lambda} ||\boldsymbol{\alpha}||_1 \tag{6.10}$$

The following expression was used for ∇f_1:

$$\begin{aligned} \nabla f_1(\boldsymbol{\alpha}) = 2\boldsymbol{\Psi}^T \int_0^{l_d} \quad & (\boldsymbol{DIDD_r}(z\mathbb{1} + \boldsymbol{\Psi\alpha}) \\ & \circ (\boldsymbol{G}\ (\boldsymbol{G}\ \boldsymbol{IDD_r}(z\mathbb{1} + \boldsymbol{\Psi\alpha}) \\ & -\boldsymbol{IDD_m}(z)))) \, dz \end{aligned} \tag{6.11}$$

where $\circ$ is the Hadamard product and $\boldsymbol{DIDD_r}$ is defined as:

$$DIDD_{r,i}(z) = \left.\frac{d}{dx} IDD_{ref}(x)\right|_{x=z} \tag{6.12}$$

and was computed by finite difference.

To increase the spatial resolution, a downsampling operator was added into Eq. 6.4:

$$\boldsymbol{IDD_m}(z) \approx \boldsymbol{D\ G\ IDD_r}(z\mathbb{1} + \boldsymbol{W}) \tag{6.13}$$

and Eq. 6.8 and the expression of its gradient were adapted accordingly.

6.2.2 Combining x-ray CT with proton radiography

In proton therapy, a x-ray CT is always acquired for treatment planning. This additional high resolution information could be used to improve the WET estimation. Nevertheless, because of the uncertainty in the conversion from HUs to RSPs and the lack of *in vivo* data, there currently does not exist any experimental high resolution WET map nor any way to accurately simulate one. With the non-unicity of the relationship between CT and WET maps, this restricts the types of methods that could be used [45].

The uncertainty on the proton range is usually considered to be around 3.5%, a significant part of which is imputed to the conversion of the planning CT into RSP which is usually done via an empirically determined relationship [37]. Assuming that a high resolution RSP map could be computed with reasonable accuracy for each patient of whom a CT would be acquired, the sought WET, W, could be expressed as the sum of the WET estimated based on the high resolution CT, WET_{CT}, and a corrective term, W_c :

$$W(x,y) = W_{CT}(x,y) + W_c(x,y) \tag{6.14}$$

With this additional information, problem 6.3 can be reformulated as follow:

$$\begin{aligned} W_{CT}^{opt}(x,y) \;=\; & W_{CT}(x,y) \\ & + \arg\min_{W_c} \sum_x \sum_y \int_0^{l_d} (IDD_m(x,y,z) \\ & - D(x,y)\,(\; G(x,y) \\ & \star IDD_r(z + W_{CT}(x,y) + W_c(x,y)))\big)^2\, dz \end{aligned} \tag{6.15}$$

Minimization of Eq. 6.15 shows similar conditioning characteristics to Eq. 6.3. To solve it, W_c may be expressed in some basis $\boldsymbol{\Psi}$ where it benefits from a sparse representation, through its coefficients α_c:

$$\boldsymbol{W_c} = \boldsymbol{\Psi \alpha_c} \tag{6.16}$$

Assuming that $\boldsymbol{W_c}$ can be sparse coded, problem 6.15 can be reformulated in a matrix-like format as:

$$\begin{aligned} \boldsymbol{\alpha_c^{opt}} \;=\; & \arg\min_{\boldsymbol{\alpha_c}} ||\boldsymbol{\alpha_c}||_0 \\ & \text{s.t.} \quad f_2(\boldsymbol{\alpha_c}) \leq \epsilon \end{aligned} \tag{6.17}$$

where $f_2(\boldsymbol{\alpha_c})$ is defined as:

$$\begin{aligned} f_2(\boldsymbol{\alpha_c}) \;=\; & \int_0^{l_d} ||\boldsymbol{IDD_m}(z) \\ & - \boldsymbol{G}\ \boldsymbol{IDD_r}(z\mathbb{1} + \boldsymbol{W_{CT}} + \boldsymbol{\Psi \alpha_c})||_2^2\, dz \end{aligned} \tag{6.18}$$

This problem can be solved similarly to Eq. 6.8 with the iterative algorithm 6.9.

6.2.3 Experimental validation

Proton radiography

The experimental validation relies on an anthropomorphic head phantom model 731-HN (CIRS, USA).

Proton radiography data were acquired with the commercially available MLIC named Giraffe (IBA, Belgium), according to the acquisition method described by Farace *et al.* [19]. The MLIC was placed at the exit side of the object that was imaged, at a short distance from its surface. To perform the acquisition, the proton therapy delivery system was operated in pencil beam scanning mode. The initial energy was 210 MeV and the spot size was 3 mm (one sigma). For each beamlet sent at a specified location, an IDD was measured by the Giraffe. Since this device has a restricted field of view (45 x 45 mm^2), a whole radiography requires several acquisitions, between each of which the object must be translated. The translations were performed by moving the couch with a distance equal to the field of view. A single direction of acquisition was considered. The gantry angle was 270° which gave a radiograph along the lateral direction.

In addition, a single energy CT scan of the head phantom was acquired at 120 kV in a 512×512 matrix, 512×512 mm^2 field of view and with a slice thickness of 1.5 mm.

Monte Carlo simulations

To test the WET estimation methods, we must have a set of proton radiographs for which the WET maps are accurately known. To do so, we decided to use simulations based on a x-ray CT of the object under consideration. The MLIC was modeled by a water tank added to the CT, at the exit side of the patient. Proton radiographs were simulated with the Monte-Carlo simulation tool named MCsquare [27]. The dose maps were exported separately for each beamlet so that the IDDs could have been later reconstructed.

In order to perfectly mimic an acquisition with the Giraffe and in particular to take into account its limited field of view, a treatment plan with a specific isocenter was made for each position at which the object should have been placed. The IDDs obtained from those simulations were then re-sampled to correspond to the depth resolution of the

Giraffe.

As for the actual measurements, the initial energy was 210 MeV and the spot size was 3 mm (one sigma). Five different spot sizes were considered: 4 mm, 5 mm, 6 mm, 7 mm and 8 mm.

To compute W, the CT was converted into RSP using the same conversion tables that were fed into MCsquare. Specifically, two tables were used by the simulation tool: one to map the HU of the CT to mass densities and one to map the HU to material compositions. The WET map corresponding to the simulation was then obtained by integrating the RSP along the path of the beamlets.

Range uncertainty model

W_{CT} was computed with a calibration curve derived from the conversion tables used for the computation of W. To introduce differences between W_{CT} and W, random variations can be added into the calibration curve [28, 12]. This was done so as to have a mean absolute relative error between 3% and 4%. For each spot spacing considered in this study, the deconvolution method was applied to ten different W_{CT}, each obtained with a randomly altered version of the calibration curve.

6.3 Results

6.3.1 Deconvolution accuracy

Fig. 6.1 shows examples of WET maps obtained with our methods, for a spot spacing of 5 mm, a value often used for integrated-mode proton imaging [41, 19, 28, 12]. For the method combining the planning CT, only one result among the ten performed experiments is illustrated. A WET map obtained from a range map estimated after a bi-cubic interpolation of the IDDs is also shown to provide a naive reference. It's hardly possible to visually distinguish between the ground truth data and the WET resulting from the sparse optimizations.

The difference between the optimized maps shown in Fig. 6.1 and the ground truth data are depicted in Fig. 6.2. Gamma index maps [3] are also presented for the sake of comparison with the state of the art method [28]. The acceptance level was a relative WET difference (RWET) of 2 % and a distance to agreement (DTA) of 2 mm. The

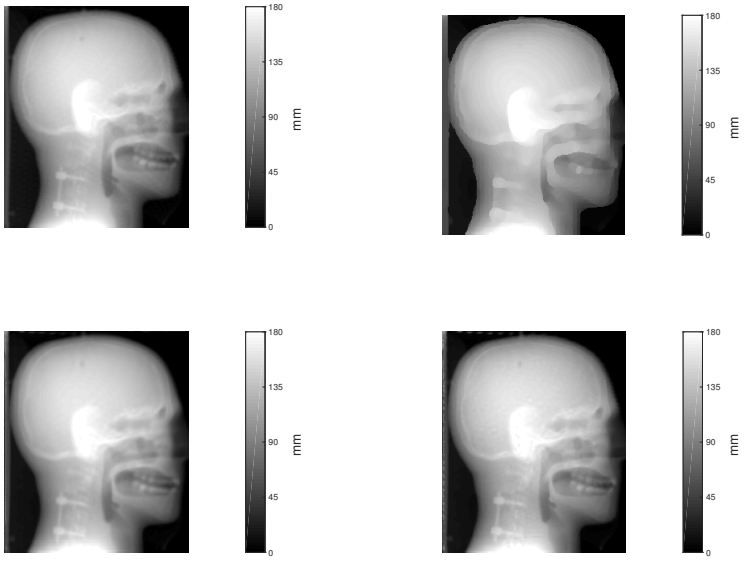

Figure 6.1: (a) Ground truth WET, W. (b) WET map obtained after converting a range map estimated from a bi-cubic interpolation of the IDDs (c) WET map determined through sparse deconvolution using the proton radiography data solely (d) WET map determined through sparse deconvolution with an estimate W_{CT} obtained using the planning CT.

passing ratio for those values was 100 % for the two method presented in this paper and for all W_{CT} considered.

Figure 6.3 shows the accuracy of the two optimization methods with respect to spot spacing. For the method combining the proton radiograph and the CT, the results of all the the ten random experiments were aggregated for each spot spacing. The errors appeared to be almost non biased since they are symmetrically distributed around null medians. This is confirmed by Fig. 6.4 which graphically shows the distributton of the WET errors for a spot spacing of 5 mm.

95% intervals are listed in Table 6.1. The accuracy is submillimeter for the second method and a spacing up to 6 mm. For the first method,

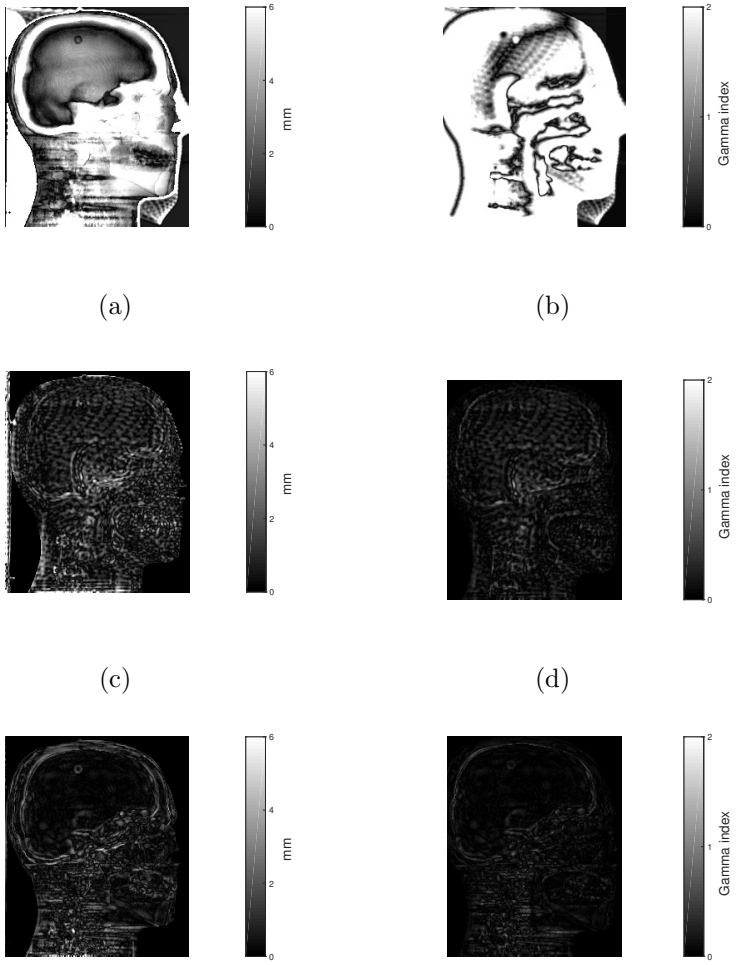

(a) (b)

(c) (d)

(e) (f)

Figure 6.2: Examples of (a) $|W - W_{CT}|$ (b) gamma index between W_{CT} and W (c) $|W - W^{opt}|$ (d) gamma index between W^{opt} and W (e) $|W - W_{CT}^{opt}|$ (f) gamma index between W_{CT}^{opt} and W.

the accuracy was better than 3 mm for spacings up to 6 mm.

The proposed method was also applied to real measurements as

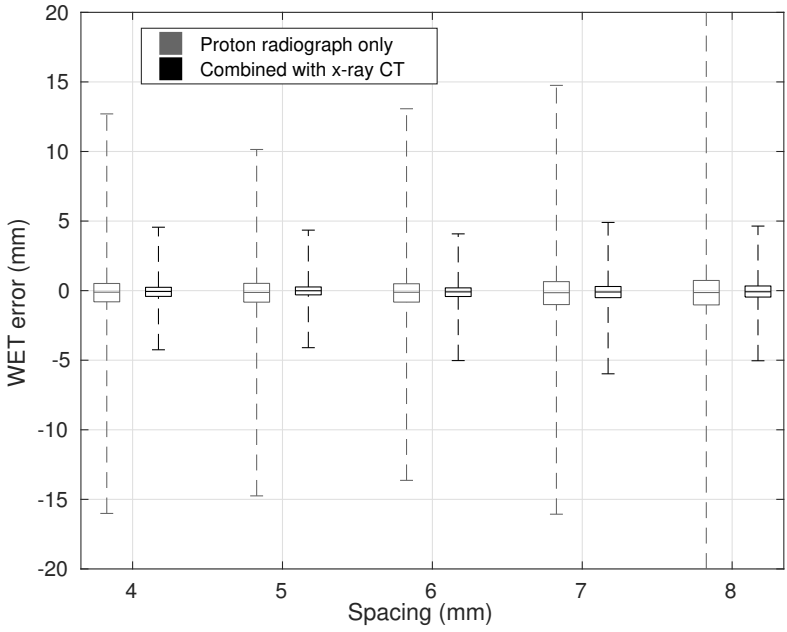

Figure 6.3: Deconvolution accuracy (absolute errors) expressed in water equivalent mm, with respect to spot spacing.

Method \Spacing (mm)	4	5	6	7	8
Proton radiograph only	2.7	2.3	2.8	3.8	4.3
Proton radiograph + CT	0.7	0.7	0.4	1.8	2.6

Table 6.1: Deconvolution accuracy (95% intervals) expressed in water equivalent mm, with respect to spot spacing.

shown in Fig. 6.5. In Fig. 6.5a-b, the WET maps obtained from the acquired proton radiograph were compared with the one estimated by our treatment planning system. First, the error on the skull, at the interface with the air, seems to suggest that there remained a residual misalignement between the CT and the acquired proton radiograph, despite an accurate kV-kV alignment manually performed before the radiography.

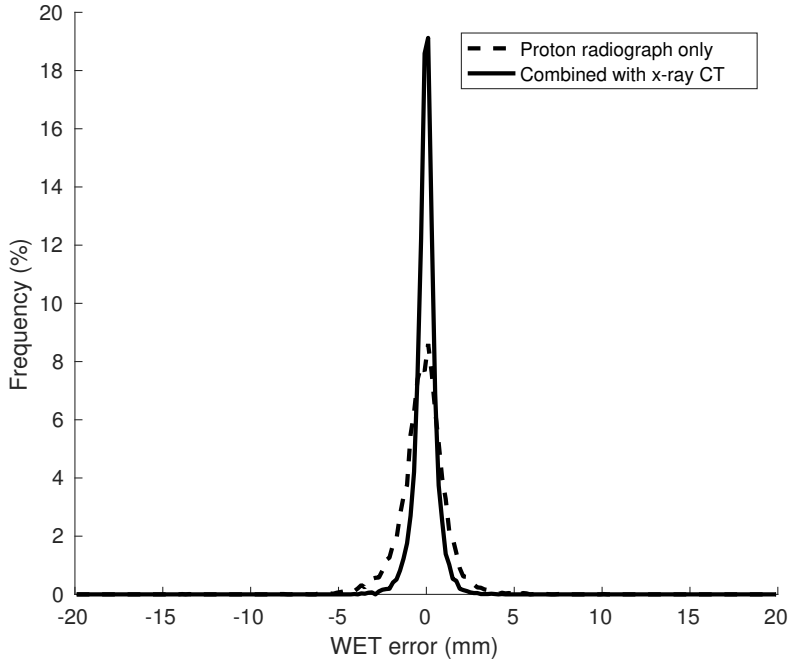

Figure 6.4: Distribution of the WET error for proton radiographs acquired with a spot spacing of 5 mm. Bin width is 0.2 mm.

The application in post-processing of the registration method proposed by Deffet *et al.* [12] significantly decreased this error, as can be seen in Fig. 6.5c-d. This is a striking example of the benefit of generating such high resolution WET maps as it clearly appears that the RSP of the titanium implant was wrongly estimated and the conversion curve to RSP could accordingly be corrected.

6.3.2 OpenREGGUI

The deconvolution methods presented in this chapter were integrated in the openREGGUI proton radiography module. In addition, a graphical user interface was created to compare WET maps and their associated proton radiographs, as shown in Fig. 6.6

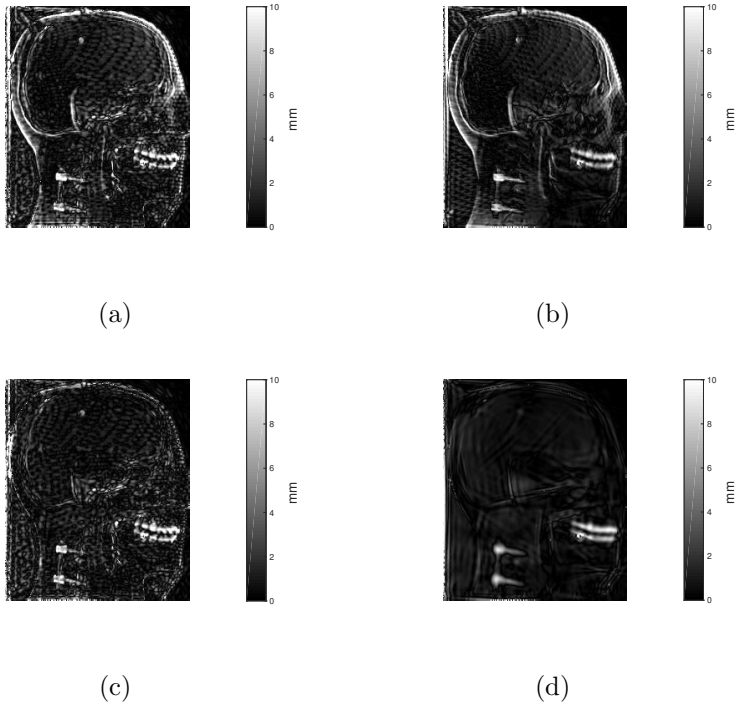

(a) (b)

(c) (d)

Figure 6.5: Absolute error maps between WET estimated from actual measurements and WET estimated based on a x-ray CT (a) from deconvolution using the proton radiograph solely (b) from deconvolution combining the proton radiograph and the x-ray CT (c) same as (a) after co-registration (d) same as (b) after co-registration.

6.4 Discussion

Range uncertainty is a crucial issue in proton therapy for which experimental data are still remarkably missing. It is usually accounted for by the use of margins during treatment planning. Among the various potential methods that could be used for *in vivo* range verification, proton radiography using a MLIC is certainly one of the easiest to enforce, which, undoubtedly, is an asset from a clinical perspective. Nevertheless, as a technique relying on dose integration, it provides data which are affected by some kind of blurring. It is a consequence of the finite

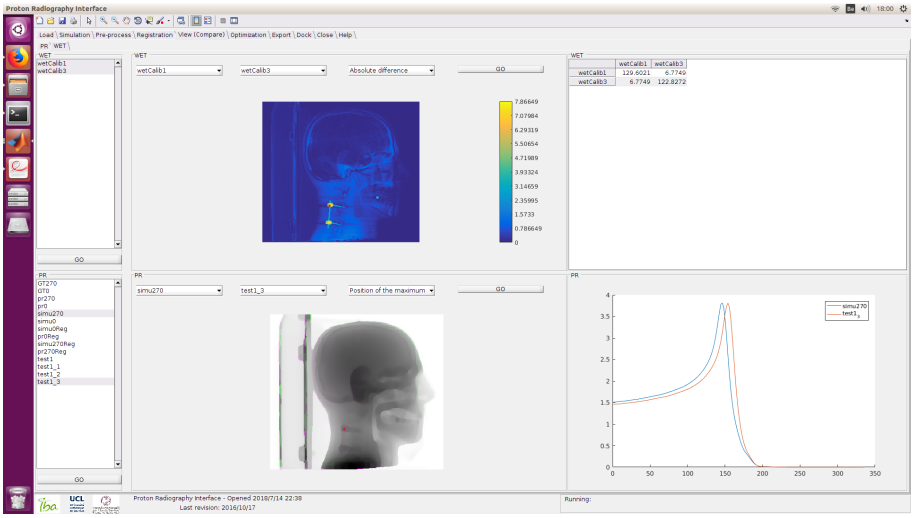

Figure 6.6: Capture of the graphical interface implemented in the openREGGUI framework to compare WET maps and associated proton radiographs.

width of the proton pencil beams.

The method to extract WET from IDD explored up to this day was relying on a linear decomposition of the curves [28]. This problem is particularly ill-posed and obviously requires some regularization to be solved. Instead, their authors proposed the linear decomposition to be followed by a demosaicing step which uses the prior information from the planning CT. This only partially copes with the non-unicity of the linear decomposition and may potentially introduce errors caused by residual misalignment between CT and proton radiography or non-bijectivity in the relationship between HU and RSP.

In the present paper, we first presented a WET estimation technique which does not require any prior information from the planning CT. Then, we showed how this method can benefit from the additional information of the planning CT which is only made possible after accurate co-registration. The technique focuses on the difference between the true WET map and the one that can be relatively well predicted with standard conversion of the HU to RSP. No additional use of this conversion is made during the optimization. This makes the deconvolution

robust against any kind of uncertainty in the conversion to RSP such as non-bijectivity of the relationship between HU and RSP, for instance.

In this paper, an experimental study was carried out on a anthropomorphic head phantom. This anatomical site is particularly well suited for proton radiography since its limited WET whatever the acquisition direction does only require moderate energy. For this phantom, the WET could be determined with less than 3 mm uncertainty (95% interval) using the proton radiography data only and a spot spacing smaller or equal to 6 mm. In a combination with the CT, the WET could be estimated with a submillimeter accuracy for spot spacing up to 6 mm. Furthermore, the error appeared to be almost non-biased. This is a key result in the context of CT conversion assessment where errors in the calibration curve generate systematic errors in the WET estimation.

The method combining x-ray CT and proton radiography is thus well suited to assess a range uncertainty usually considered to be around 3.5% of the nominal range. Moreover, the largest discrepancies were located in area presenting a high level of lateral inhomogeneities. It would not actually be appropriate to consider those areas when assessing range uncertainty because of the dependence of their WET to the smallest misalignment.

The spot spacing that can be used is 6 mm maximum. This value also leads to a co-registration with a high level of accuracy [13]. Thus, the spatial resolution of the WET map can be much better than the spot spacing, limiting the dose to be delivered to the patient.

6.5 Conclusions

In this chapter, we have developed an algorithm to estimate WET maps from integrated-mode proton radiography data in combination with a x-ray CT. It was tested with Monte Carlo simulations and measurements performed with the Giraffe. WET maps with pixels of 1×1mm were estimated from proton radiographs acquired with spot spacings ranging from 4 mm to 8 mm. The larger spot spacing that can be used while maintaining submillimeter accuracy is 6 mm, thus decreasing the delivered dose by 36.

Such a WET-map could be used to assess the RSP computation in a comparison with the one that could be computed by the treatment

planning system. Our experimental validation showed that this kind of comparison can be impacted by residual set-up errors which were correctly mitigated by applying the registration method for proton radiography data proposed by Deffet *et al.* [12].

Chapter 7

On the use of proton radiography to improve CT conversion

7.1 Introduction

7.1.1 The role of the planning CT

In proton therapy, treatment planning requires a 3D map of the relative proton stopping powers (RSP) of the patient. Ideally, this would be obtained through proton computed tomography. Although an increasing number of groups worldwide are investigating 3D proton imaging, there exists no commercial system yet. Therefore, the current approach consists in acquiring a CT scan of the patient and then convert it into RSP. Unfortunately, this conversion is tainted by uncertainties which approximately represent 1.8% of the 3.5% treatment margins that are commonly used [58, 37]. The main reason arises from the differences between the physical properties on which rely x-ray attenuation coefficients on the one hand and proton stopping powers on the other hand. Whereas the linear attenuation coefficient is a function of the electron density and the cross sections, the proton stopping power depends on the electron density and the mean excitation energy of the tissue.

In proton therapy, RSP computation is usually done through the approximated Bethe-Bloch formula, of which the use was first proposed

by Schneider at al [43]:

$$RSP = \rho_{e,t} \frac{\ln\left(2m_e c^2 \beta^2 / I_t (1-\beta^2)\right) - \beta^2}{\ln\left(2m_e c^2 \beta^2 / I_w (1-\beta^2)\right) - \beta^2} \tag{7.1}$$

where $\rho_{e,t}$ is the relative electron density of the tissue, m_e is the mass of the electron, β is the relative speed of the incident protons, I_t is the mean excitation energy of the tissue and I_w is the mean excitation energy of water.

Fig. 7.1 shows a typical relationship between Hounsfield units (HU) and RSPs for human tissues of which the compositions taken from the ICRU44 report [22] are listed in Table 7.1. It strikingly shows that there is actually no bijective relationship between HU and RSP. Moreover, because HUs depend on the spectrum of the CT scanner, such a calibration curve must be specifically established for each machine used for treatment planning. In the case of Fig. 7.1, a typical x-ray spectrum was generated by Spektr [24] for a tube voltage of 120 kVP.

Attenuation coefficients of tissues, named μ_t are related to the atomic composition of tissues according to the following formula:

$$\mu_t(E) = \rho_t N_A \sum_i^N w_i \frac{Z_i}{A_i} \sigma_{e,i}(E) \tag{7.2}$$

where ρ_t is the mass density, N_A is th Avogadro number, N is the largest atomic number of elements present in the tissues, w_i is the mass fraction of element i in the tissue, Z_i is the atomic number, A_i is the atomic mass and $\sigma_{e,i}$ is the (per) electron cross section of element i of which the values used to generate Fig. 7.1 were found in the XCOM database [33].

In the case of Fig. 7.1, proton RSP were computed according to Eq. 7.1 and the Bragg additivity rule for mean excitation energies:

$$\ln I_t = \frac{\sum_i^N w_i \frac{Z_i}{A_i} \ln I_i}{\sum_i^N w_i \frac{Z_i}{A_i}} \tag{7.3}$$

where I_i is the mean excitation energy of element i.

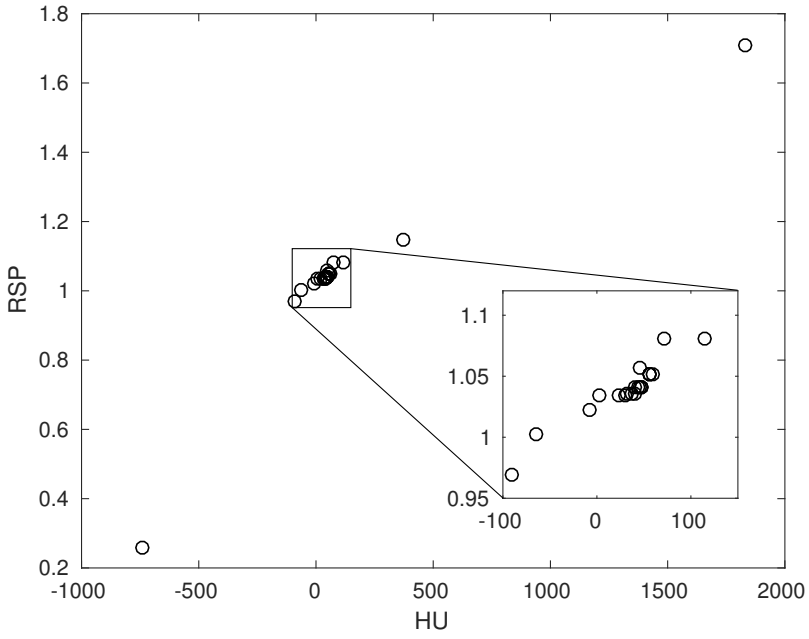

Figure 7.1: Relationship between HU and RSP theoretically computed for the list of tissues of ICRU report 44.

Material	ρ	H	He	C	N	O	Na	Mg	P	S	Cl	K	Ca	Fe
Adipose	0.95	11.4	0	59.8	0.7	27.8	0.1	0	0	0.1	0.1	0	0	0
Eye lens	1.07	9.6	0	19.5	5.7	64.6	0.1	0	0.1	0.3	0.1	0	0	0
Liver	1.06	10.2	0	13.9	3	71.6	0.2	0	0.3	0.3	0.2	0.3	0	0
Lung (deflated)	1.05	10.3	0	10.5	3.1	74.9	0.2	0	0.2	0.3	0.3	0.2	0	0
Lung (inflated)	0.26	10.3	0	10.5	3.1	74.9	0.2	0	0.2	0.3	0.3	0.2	0	0
Muscle (skeletal)	1.05	10.2	0	14.3	3.4	71	0.1	0	0.2	0.3	0.1	0.4	0	0
Ovary	1.05	10.5	0	9.3	2.4	76.8	0.2	0	0.2	0.2	0.2	0.2	0	0
Skeleton (red marrow)	1.03	10.5	0	41.4	3.4	43.9	0.1	0	0.2	0.2	0.2	0	0	0.1
Skin	1.09	10	0	20.4	4.2	64.5	0.2	0	0.1	0.2	0.3	0.1	0	0
Testis	1.04	10.6	0	9.9	2	76.6	0.2	0	0.1	0.2	0.2	0.2	0	0
Thyroid	1.05	10.4	0	11.9	2.4	74.5	0.2	0	0.1	0.1	0.2	0.1	0	0
Skeleton (cortical bone)	1.92	3.4	0	15.5	4.2	43.5	0.1	0.2	10.3	0.3	0	0	22.5	0
Blood (whole)	1.06	10.2	0	11	3.3	74.5	0.1	0	0.1	0.2	0.3	0.2	0	0.1
Brain	1.04	10.7	0	14.5	2.2	71.2	0.2	0	0.4	0.2	0.3	0.3	0	0
Breast (mammary gland)	1.02	10.6	0	33.2	3	52.7	0.1	0	0.1	0.2	0.1	0	0	0
GI tract (intestine)	1.03	10.6	0	11.5	2.2	75.1	0.1	0	0.1	0.1	0.2	0.1	0	0
Heart (blood filled)	1.06	10.3	0	12.1	3.2	73.4	0.1	0	0.1	0.2	0.3	0.2	0.1	0
Kidney	1.05	10.3	0	13.2	3	72.4	0.2	0	0.2	0.2	0.2	0.2	0.1	0
Lymph	1.03	10.8	0	4.1	1.1	83.2	0.3	0	0	0.1	0.4	0	0	0
Pancreas	1.04	10.6	0	16.9	2.2	69.4	0.2	0	0.2	0.1	0.2	0.2	0	0
Skeleton (cartilage)	1.1	9.6	0	9.9	2.2	74.4	0.5	0	2.2	0.9	0.3	0	0	0
Skeleton (spongiosa)	1.18	8.5	0	40.4	2.8	36.7	0.1	0.1	3.4	0.2	0.2	0.1	7.4	0.1
Skeleton (yellow marrow)	0.98	11.5	0	64.4	0.7	23.1	0.1	0	0	0.1	0.1	0	0	0
Spleen	1.06	10.3	0	11.3	3.2	74.1	0.1	0	0.3	0.2	0.2	0.3	0	0

Table 7.1: Mean composition of typical human tissues. Source: [22].

7.1.2 CT conversion methods

Tissue surrogate calibration

The most straightforward method to convert a x-ray CT into proton RSPs relies on the use of tissue surrogates to derive an empirical relationship. It is a three-step method:

1. The HU of the tissue surrogates are experimentally measured with the CT scanner.
2. The corresponding RSP are determined. This can be done experimentally with the ion line. Alternatively, the RSP can also be theoretically computed based on the elemental compositions of the surrogates, using Eq. 7.1.
3. The conversion curve is obtained by plotting the measured HUs vs. the RSPs and by interpolating between those points.

This straightforward method, however, presents a major drawback which arises from the non-bijectivity of the HU-RSP relationship [43]. Surrogates manufacturers design them so that they exhibit the same attenuation characteristics for a given energy range and so that they show similar physical properties such as mass and density. Nonetheless, because the surrogates atomic compositions differ from those of real tissues, their attenuation characteristics cannot be identical for the entire energy range used in radiation therapy and particularly for low energy x-rays and high energy protons [59].

Stoichiometric calibration

To overcome this problem, Schneider [43] proposed an indirect method to establish the HU-RSP curve, the so-called stoichiometric calibration. The method is composed of four steps:

1. Parametrize the response of the CT scanner using the following equation:
$$HU = \rho_{e,t} \left(AZ^{3.62} + BZ^{1.86} + C \right) \tag{7.4}$$
where Z is the effective atomic number. Constants A, B, C are determined by a least-square minimization with measured HUs of materials of known chemical compositions.

2. Predict HUs of human tissues with Eq. 7.4 using tables of chemical compositions from the literature such as Woodard and White [56], White *et al.* [54], and ICRU [22].

3. Predict RSPs of human tissues with Eq. 7.1 using the same tables of chemical compositions.

4. Plot the HUs vs. the RSPs and interpolate between the points.

7.1.3 Range uncertainty in CT conversion

The majority of conversion methods from single energy CT to RSP rely on a piecewise linear curve. As stated above, various sources of uncertainties interfere in this process.

First, the relationship between HU and RSP is clearly not bijective.

Secondly, the relevance of the model depends on the materials used to establish the curve. In the so-called stoichiometric calibration, tables of mean composition of human tissues are used. The atomic content of patient tissues may differ, however. Small variations in elemental compositions and in mass density were shown to significantly change CT numbers [57]. Since single energy CT cannot be used to obtain both information, it limits the precision to which tissues can be resolved. Consequently, this limitation is also reflected into the stoichiometric calibration.

Finally, inconsistencies and approximations in the mean excitation energies may also impact the conversion. Their values differ depending on the source ([8, 23, 25]. Furthermore the recommended value for the mean excitation energy of water has changed many times over the past decades [8, 23, 30, 38, 16, 5]. Any inconsistency between values used for water and tissues can contribute to the errors in RSP estimation up to 3% [5, 37, 50].

7.1.4 Patient-specific calibration curves

One of the initial aim of proton radiography was to generate patient-specific calibration curve [42, 15] so that the residual range error would be minimized. Several authors proposed optimization methods to finely tune piecewise linear curves [15, 10, 4], in the context of treatment planning based on single energy CT. Nevertheless, we believe that these

state-of-the-art methods only work under limited conditions which are rarely met in a real patient.

In this chapter, we present a theoretical study that brings to light important limitations that were not considered by the authors. We consider an anthropomorphic head phantom. This anatomical site is particularly well suited for proton radiography thanks to its limited water equivalent path length (WEPL) whatever the direction of acquisition.

7.2 Materials and Methods

7.2.1 An overview of optimization methods

The type of calibration curve considered in this paper is a piecewise linear function of the HU. The points of interpolation are named $(HU_{int,i}, RSP_{int,i})$ or in vector format $(\boldsymbol{HU_{int}}, \boldsymbol{RSP_{int}})$ and the interpolation function is refered to as $f_{\boldsymbol{HU_{int}},\boldsymbol{RSP_{int}}} : \Omega_{HU} \rightarrow \Omega_{RSP} : HU \mapsto f_{\boldsymbol{HU_{int}},\boldsymbol{RSP_{int}}}(HU)$ where Ω_{HU} and Ω_{RSP} are the sets of possible values for HUs and RSPs, respectively.

Doolan's optimization

Doolan *et al.* first proposed a method to optimize the calibration curve [15]. They sought the values of $\boldsymbol{RSP_{int}}$ that would minimize the difference between predicted WEPLs, named $WEPL_{plan}$ and measured WEPLs, named $WEPL_m$:

$$\begin{aligned}\boldsymbol{RSP}_{\boldsymbol{int}}^{opt} = \arg\min_{\boldsymbol{RSP_{int}}} \sum_{x,y} \left(\sum_{z} f_{\boldsymbol{HU_{int}},\boldsymbol{RSP_{int}}}(HU(x,y,z)) s_z \right. \\ \left. - WEPL_m(x,y) \right)^2 \\ = \arg\min_{\boldsymbol{RSP_{int}}} \sum_{x,y} \left(WEPL_{plan}(x,y) - WEPL_m(x,y) \right)^2 \end{aligned} \quad (7.5)$$

where s_z is the voxel thickness.

Collins-Fekete's optimization

Since f is a piecewise linear function, Eq. 7.5 can also be written:

$$\boldsymbol{RSP}_{\boldsymbol{int}}^{opt} = \arg\min_{\boldsymbol{RSP_{int}}} ||\boldsymbol{A_{int}}\ \boldsymbol{RSP_{int}} - \boldsymbol{WEPL_m}||_2^2 \quad (7.6)$$

where $\boldsymbol{A_{int}}$ represents the total length crossed by the protons in each $\boldsymbol{HU_{int,i}}$. This alternative formulation was introduced by Collins-Fekete *et al.* in the context of list-mode proton radiography [10].

Albert's optimization

Very recently, Albert *et al.* proposed a third method [4] in a study based on prompt gamma data. However, the method itself does not restrict to prompt gamma only and can be adapted to any kind of *in vivo* range verification technique, including proton radiography.

The cost function they use is the squared difference between measured ranges and predicted ones. Moreover, they assume that the difference between the calibration curve used for treatment planning and the ideal one is a piecewise linear function of the HU. The points of interpolation of the corrective function are named $(HU_{\phi,i}, RSP_{\phi,i})$ or in vector format $(\boldsymbol{HU_\phi}, \boldsymbol{RSP_\phi})$. Therefore, we can write

$$\boldsymbol{WEPL}^{opt} = \boldsymbol{A}_{int}\boldsymbol{RSP_{int}} + \boldsymbol{A}_{\phi}\boldsymbol{RSP}_{\phi}^{opt} \tag{7.7}$$

This is obviously equivalent to the two previous techniques mentioned above but Albert's work extended its applicability to other *in vivo* range verification techniques such as prompt gamma imaging.

He first approximated the difference between the predicted range, named R_{plan}, and the measured one, named R_m, as:

$$R_{plan}(x,y) - R_m(x,y) = \frac{WEPL_{true}(x,y,R_{phys}) - WEPL_{true}(x,y,R_{plan})}{\frac{\partial W_{true}(x,y,z)}{\partial z}\big|_{z=R_{plan}}} \tag{7.8}$$

where $WEPL_{true}$ is the actual WEPL an R_{phys} is the actual range.

Nevertheless, in proton radiography, the exact expression can be used, assuming that the detector is calibrated in water :

$$\begin{aligned} R(x,y) - R_m(x,y) =& WEPL_{true}(x,y,R_{phys}) \\ & - WEPL_{true}(x,y,R_{plan}) \\ =& WEPL_{true}(x,y,z_{patient\ surf.}) \\ & - WEPL_{plan}(x,y,z_{patient\ surf.}) \\ =& WEPL_m(x,y,z_{patient\ surf.}) \\ & - WEPL_{plan}(x,y,z_{patient\ surf.}) \end{aligned} \tag{7.9}$$

where $WEPL_{plan}$ is the predicted WEPL. This can be re-written in a matrix-like format :

$$\boldsymbol{R} - \boldsymbol{R_m} \;=\; \boldsymbol{A_\phi}\ \boldsymbol{RSP_\phi} \tag{7.10}$$

which again shows the equivalence with previous methods.

The last step was an approximation of Eq. 7.10 in powers of $\boldsymbol{RSP_\phi}$ but this is not necessary for proton radiography since this equation is a linear system which can be solved directly.

Variant

In proton radiography using a multi-layer ionization chamber, the determination of the WEPL map from the measured integral depth-dose profiles (IDD) might be computationally expensive [13]. In certain circumstances, it might be profitable to perform the optimization directly on raw data:

$$\begin{aligned}\boldsymbol{RSP_\phi^{opt}} \;=\; & \arg\min_{\boldsymbol{RSP_\phi}} ||\boldsymbol{IDD_m} - \boldsymbol{G}\ \boldsymbol{IDD}\,(\boldsymbol{A_{int}}\ \boldsymbol{RSP_{int}} \\ & +\ \boldsymbol{A_\phi}\ \boldsymbol{RSP_\phi})||_2^2 \end{aligned} \tag{7.11}$$

where $\boldsymbol{IDD_m}$ are the measured IDDs, $\boldsymbol{G}$ is the circulant matrix associated with the bi-dimensional Gaussian convolution kernel of which the sigmas equal those of the beam. The drawback of this method, however, resides in the potential non-convexity of the cost function.

7.2.2 Stability

We showed that Doolan's, Collins-Fekete's and Albert's cost functions are mathematically equivalent in the context of proton radiogrpahy. The formalism used hereafter is the one of Collins-Fekete.

Matrix $\boldsymbol{A_{int}}$ $(m \times n)$ may be expressed through a singular value decomposition:

$$\boldsymbol{A_{int}} = \boldsymbol{USV^*} \tag{7.12}$$

where $\boldsymbol{U}$ $(m \times m)$ and $\boldsymbol{V}$ $(n \times n)$ are unitary matrices and $\boldsymbol{S}$ $(m \times n)$ is a diagonal matrix of which the diagonal elements are the singular values

of $\boldsymbol{A_{int}}$. If the number of non-zero singular values of $\boldsymbol{A_{int}}$ is n, then the solution to problem 7.6 is unique and is given by:

$$\boldsymbol{RSP_{int}^{opt}} = \boldsymbol{A_{int}^{+}} \boldsymbol{WEPL_m} \tag{7.13}$$

where $\boldsymbol{A_{int}^{+}} = (\boldsymbol{A_{int}^{*}} \boldsymbol{A_{int}})^{-1} \boldsymbol{A_{int}^{*}}$ is the generalized inverse matrix.

On the contrary, if at least one singular value of $\boldsymbol{A_{int}}$ is null, the determinant of $(\boldsymbol{A_{int}^{*}} \boldsymbol{A_{int}})$ is null and there exists an infinity of solutions.

During the optimization, at least four sources of errors may be encountered:

- Uncertainty in the $WEPL$ measurement;
- CT noise and reconstruction artefacts;
- Difference in the anatomy of the patient between the CT image and the proton radiograph;
- Misalignment between the CT image and the proton radiograph.

The first source of uncertainty may be modelled as a perturbation, named $\boldsymbol{\delta_{WEPL}}$, of the $\boldsymbol{WEPL_m}$ vector. The three other sources correspond to a perturbation $\boldsymbol{\delta_A}$ of matrix $\boldsymbol{A_{int}}$. Considering those perturbations separately, we can show (see appendix A for proof) that:

$$\frac{||\boldsymbol{\delta_{RSP}}||_2}{||\boldsymbol{RSP_{int}}||_2} \leq \frac{|||\boldsymbol{A_{int}^{+}}||| \; ||\boldsymbol{WEPL_m}||_2}{||\boldsymbol{A_{int}^{+}} \boldsymbol{WEPL_m}||_2} \; \frac{||\boldsymbol{\delta_{WEPL}}||_2}{||\boldsymbol{WEPL_m}||_2} \tag{7.14}$$

and

$$\frac{||\boldsymbol{\delta_{RSP}}||_2}{||\boldsymbol{RSP_{int}}||_2} \leq \frac{|||\boldsymbol{A_{int}^{+}}|||^2 \; |||\boldsymbol{A_{int}}|||}{1 - |||\boldsymbol{\delta_A} \boldsymbol{A_{int}^{+}}|||} \; \frac{||\boldsymbol{WEPL_m}||_2}{||\boldsymbol{A_{int}^{+}} \boldsymbol{WEPL_m}||_2} \; \frac{|||\boldsymbol{\delta_A}|||}{|||\boldsymbol{A_{int}}|||} \tag{7.15}$$

where $|||.|||$ is the operator norm defined as:

$$|||A||| = \sup_{\boldsymbol{x} \in \mathbb{R}^n \setminus \{0\}} \frac{||Ax||_2}{||x||_2} \tag{7.16}$$

Moreover, inequation. 7.14 may be reformulated in a form similar to inequation. 7.15:

$$\begin{aligned}\frac{||\boldsymbol{\delta_{RSP}}||_2}{||\boldsymbol{RSP_{int}}||_2} &\leq \frac{|||\boldsymbol{A_{int}^+}||| \; ||\boldsymbol{WEPL_m}||_2}{||\boldsymbol{A_{int}^+ WEPL_m}||_2} \frac{|||\boldsymbol{A_{int}^+ A_{int}}|||}{1-|||\boldsymbol{\delta_A A_{int}^+}|||} \frac{||\boldsymbol{\delta_{WEPL}}||_2}{||\boldsymbol{WEPL_m}||_2} \\ &\leq \frac{|||\boldsymbol{A_{int}^+}|||^2 \; |||\boldsymbol{A_{int}}|||}{1-|||\boldsymbol{\delta_A A_{int}^+}|||} \frac{||\boldsymbol{WEPL_m}||_2}{||\boldsymbol{A_{int}^+ WEPL_m}||_2} \frac{||\boldsymbol{\delta_{WEPL}}||_2}{||\boldsymbol{WEPL_m}||_2}\end{aligned} \tag{7.17}$$

Therefore, an upper bound of the relative variation of the norm of the $\boldsymbol{RSP_{int}}$ with respect to those of $\boldsymbol{A_{int}}$ and $\boldsymbol{WEPL_m}$ is proportional to $\frac{|||\boldsymbol{A_{int}^+}|||^2 \; |||\boldsymbol{A_{int}}|||}{1-|||\boldsymbol{\delta_A A_{int}^+}|||} \frac{||\boldsymbol{WEPL_m}||_2}{||\boldsymbol{A_{int}^+ WEPL_m}||_2}$.

7.2.3 Experimental data

Our study relies on the case of an anthropomorphic head phantom model 731-HN (CIRS, USA). A single energy CT scan of this phantom was acquired at 120 kV in a 512×512 matrix, 512×512 mm^2 field of view and with a slice thickness of 1.5 mm. The CT was later resampled on a $1 \times 1 \times 1$ mm grid by linear interpolation.

A single direction of acquisition was considered. The gantry angle was 270°. This gave a radiograph along the lateral direction. The spot spacing was 5 mm and the proton acquisition grid contained 45×64 spots, as shown in fig. 7.2.

We assume that the noise in the WEPL estimation is normally distributed:

$$WEPL_m(x,y) = \sum_z RSP(HU(x,y,z)) \; s_z + WEPL_{noise} \tag{7.18}$$

where s_z is the voxel thickness and $WEPL_{noise}$ is a normally distributed random variable of zero mean and standard deviation σ_{noise}.

The generic calibration curve shown in Fig. 7.3 was used to construct vector $\boldsymbol{HU_{int}}$ and to simulate the proton radiograph based on the CT.

Matrix $\boldsymbol{A_{int}}$ was built from the CT data and the spots position

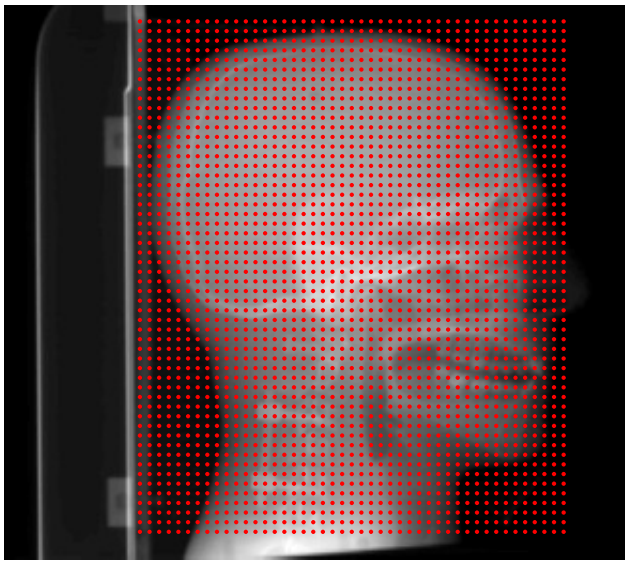

Figure 7.2: Head phantom and spot map (red dots) considered in the experimental study.

using:

$$A_{int_{i,j}} = \left(\sum_{HU \in S_{ij}} \frac{HU - HU_{int,j}}{HU_{int,j+1} - HU_{int,j}} + \sum_{HU \in S_{ij-1}} \left(1 - \frac{HU - HU_{int,j-1}}{HU_{int,j} - HU_{int,j-1}} \right) \right) s_z \quad (7.19)$$

where S_{ij} is the set of CT voxels traversed by beamlet i such that $HU_{int,j} \leq HU < HU_{int,j+1}$ and S_{ij-1} is the set of CT voxels traversed by beamlet i such that $HU_{int,j-1} \leq HU < HU_{int,j}$.

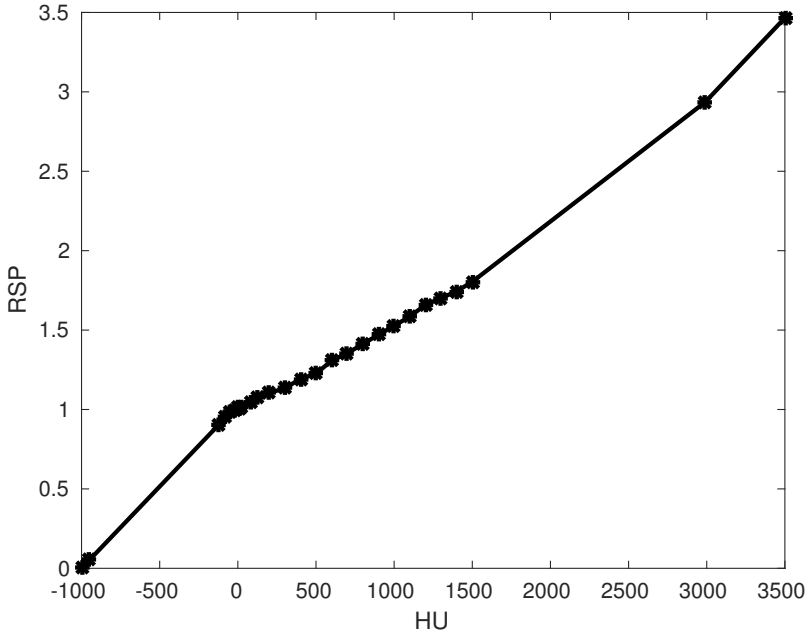

Figure 7.3: Generic calibration curve composed of 26 linear segments.

7.3 Results

The proton radiograph was simulated with a map of 45×64 spots and the the calibration curve had 27 interpolation points. Hence, the size of matrix $\boldsymbol{A_{int}}$ was 2430×27. The solution in the case of $\sigma_{noise} = 0$ perfectly coincided with the generic calibration curve. The rank of $\boldsymbol{A_{int}}$ was indeed 27.

If $\boldsymbol{\delta_{WEPL}} = \boldsymbol{WEPL_{noise}}$ with $\sigma_{noise} = 1$ for instance, $||\boldsymbol{\delta_{WEPL}}||$ behaves according to a χ distribution of which the mean and variance are [53]:

$$\mu = \sqrt{2}\frac{\Gamma\left(\frac{n+1}{2}\right)}{\Gamma\left(\frac{n}{2}\right)} \tag{7.20}$$

and

$$\sigma^2 = 2\frac{\Gamma\left(\frac{n}{2}\right)\Gamma\left(1+\frac{n}{2}\right) - \Gamma^2\left(\frac{n+1}{2}\right)}{\Gamma^2\left(\frac{n}{2}\right)} \tag{7.21}$$

where Γ is the gamma function:

$$\Gamma(z) = \int_0^\infty x^{z-1} e^{-x} dx \tag{7.22}$$

In this case, $\mu = 49.29$ and $\sigma^2 = 0.5$. Moreover $||WEPL_m|| = 5251.2$. Consequently, inequation 7.14 yields, in this case, to

$$\frac{||\boldsymbol{\delta_{RSP}}||}{||\boldsymbol{RSP_{int}}||} \leq 60.0 \tag{7.23}$$

In other words, $||\boldsymbol{\delta_{RSP}}||$ may possibly be 60.0 times higher than $||\boldsymbol{RSP}||$. Nonetheless, this corresponds to a worst case situation that might never happen. Twenty-five experiments were run with $\sigma_{noise} = 1$ (mm) and the optimized curves are shown in Fig. 7.4. They significantly differs from the generic one. The mean value of $\frac{||\boldsymbol{\delta_{RSP}}||}{||\boldsymbol{RSP_{int}}||}$ was 9% and the standard deviation 5%.

A similar experiment was conducted with the assumption that the WEPL measurement can be carried out with an accuracy of 1% (95% interval). Hence $\sigma_{noise} = \frac{1}{1.96}\%$. Results are shown in Fig. 7.5.

To analyze perturbation on matrix $\boldsymbol{A_{int}}$, we decided to consider its singular value decomposition (Eq. A.2). A plot of the singular values, S_i, is shown in Fig. 7.6. The five highest S_i are several orders of magnitude higher than the others. Matrix $\boldsymbol{A_{int}}$ could be approximated by keeping only the highest singular values. The approximated matrix is hereafter referred to as $\widetilde{\boldsymbol{A_{int}}}$. For this example, we chose to keep the twenty highest S_i. This led to:

$$\frac{||\boldsymbol{A_{int}}|| - ||\widetilde{\boldsymbol{A_{int}}}||}{||\boldsymbol{A_{int}}||} = 8.6641\ 10^{-6} \tag{7.24}$$

and

$$\frac{||\boldsymbol{A_{int}} - \widetilde{\boldsymbol{A_{int}}}||}{||\boldsymbol{A_{int}}||} = 0.0042 \tag{7.25}$$

In other words, this simplification in the spectral content of $\boldsymbol{A_{int}}$ only very slightly changed its Frobenius norm. However, it had a huge consequence on the solution of problem 7.6. Because the rank of $\boldsymbol{A_{int}}$ was 20 after approximation, there were an infinite number of solutions to the least-square problem. Actually, seven $RSP_{int,i}$ cannot be determined.

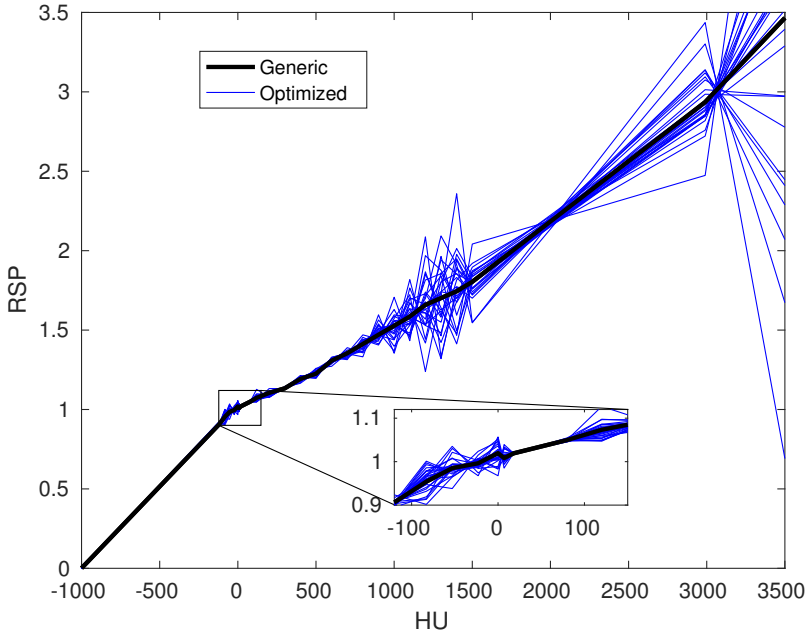

Figure 7.4: Calibration curves resulting from optimizations performed on altered WEPL map ($\sigma_{noise} = 1$ (mm)).

If those variables are set to 0 for instance, the calibration curve shown in Fig. 7.7 is obtained. This choice is arbitrary and other values would have led to a different curve.

Eq. 7.24 and 7.25 showed that small changes in matrix $\boldsymbol{A_{int}}$ could have dramatic consequences on the solution. Actually, Fig. 7.6 shows that a system with matrix $\boldsymbol{A_{int}}$ is close to under-determination.

7.4 Discussion

By providing a direct information about the energy loss of protons through the patient, proton radiography offers the potential to correct the conversion of planning CT. In 2015, Doolan *et al.* proposed a method to establish a patient specific calibration curve based on WEPL maps [15]. The authors demonstrated the robustness of their optimiza-

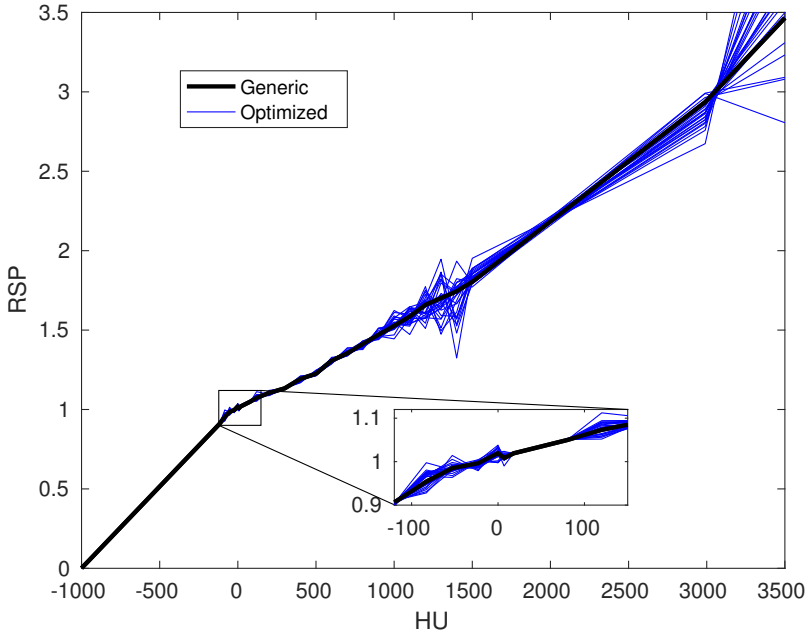

Figure 7.5: Calibration curves resulting from optimizations performed on altered WEPL map ($\sigma_{noise} = 1/1.96\%$).

tion with respect to CT noise and measurement uncertainties. Later, Collins-Fekete *et al.* proposed a similar technique for list-mode proton radiography [10]. Finally, Albert *et al.* developed an optimization method working with most of *in vivo* range verification techniques including prompt-gamma imaging and proton radiography.

In this chapter, we first demonstrated the mathematical equivalence between the three methods mentioned above, in the case of proton radiography. However, their respective authors came to different conclusions. Doolan judged he could decrease the range uncertainty by a few tenths of a percent. On the contrary, Collins-Fekete determined calibration curves with local errors up to a few percents for the case of anthropomorphic phantoms. Finally, Albert obtained similar results on curves optimized using prompt gamma data.

In the previous section, we showed that the optimization problem

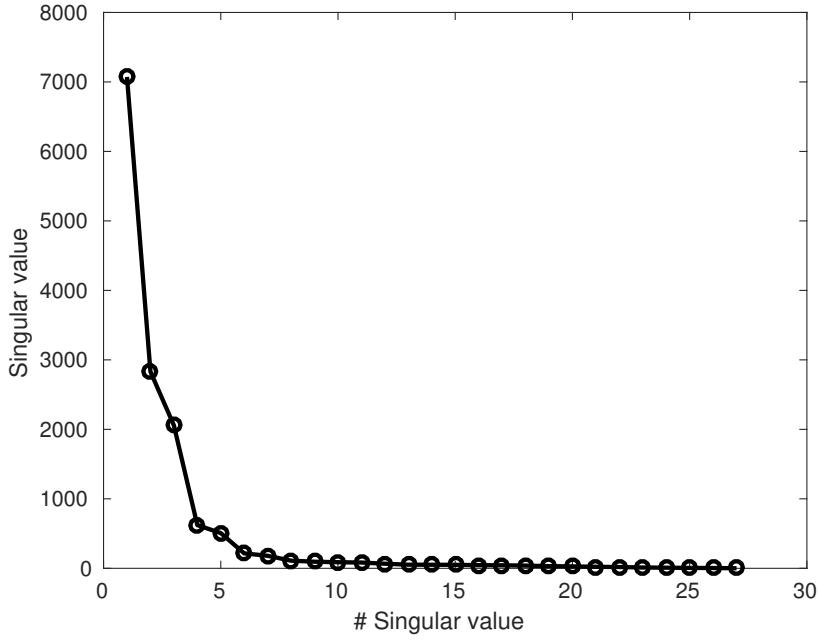

Figure 7.6: Singular values of matrix $\boldsymbol{A_{int}}$ sorted by magnitude.

may be particularly ill-posed. This characteristics was not studied with details by the authors mentioned above although Doolan performed two robustness analyses with respect to noise in CT and in proton radiographs. His work actually had flaws that should be discussed. First, to study the impact of multiple Coulomb scattering (MCS) on the optimizer, he considered an artificial phantom made out of uniform blocks having a thickness of 5 cm, arranged in four rows. It artificially gave an excellent conditioning to system 7.6 which was far from the very poor one encountered with real anatomy. As a result, what he solved was a perfectly conditioned least-square problem. Secondly, the robustness analysis with respect to CT noise was on the contrary based on an anthropomorphic CT but the organs were overridden by four different HU: bladder HU=0, prostate HU=58, muscle HU=66, rectum HU=66, cortical bone HU=1194. This again significantly changed the content of matrix $\boldsymbol{A}$. Then, CT noise was modelled as a random variable of

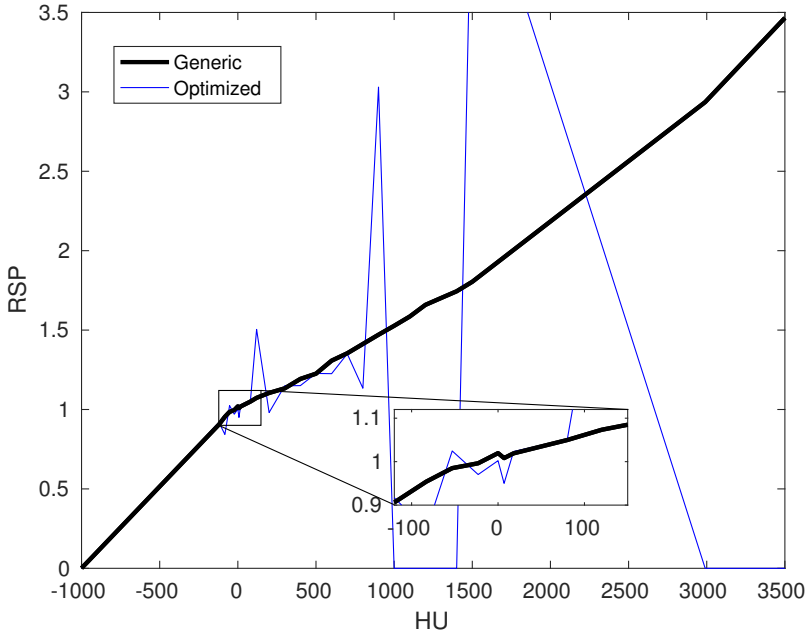

Figure 7.7: Calibration curve resulting from an optimization performed with an approximation of rank 20 of matrix $\boldsymbol{A_{int}}$ (initially of rank 27) and from setting the seven undetermined variables to 0.

zero mean and standard deviation, named σ_{noise}, ranging from 1% to 10% of the HU value. Because the relationship between HUs and RSPs was piecewise linear, RSPs exhibited the same uncertainty. The final uncertainty on the WEPL was thus of zero mean and standard deviation $\sigma_{noise}/\sqrt{N}$ (%) where N was the number of voxels traversed by the protons. For instance, if there were 100 voxels, the standard deviation of the WEPL would have been comprised between 0.1% and 1%. Moreover, having overwritten HU with a limited amount of values altered the validity of the noise model. In practice, the combination of CT noise and the piecewise property of the curve lead to a bias in the estimation of the RSP, even if noise is symmetric, as shown by Brousmiche *et al.* [9].

To restrict the solution domain, regularization or hard constraints could be used. Doolan and Albert imposed the monotonicity of the

curve which is questionable because the relationship between HU and RSP does not theoretically respect this assumption, as shown in Fig. 7.1. Secondly, Albert bounded the values that could be taken by $\boldsymbol{RSP}_{\phi}$. Yet this restricts the domain of the solution, it does not necessarily solve the unicity issue.

Since the conditioning of Eq. 7.7 depends on the choice of $\boldsymbol{HU}_{\phi}$, it might be possible to find a sampling which would guarantee the unicity of the solution but this, of course, also depends on the anatomy being considered. Trivially, if $\boldsymbol{HU}_{\phi}$ only contains one single point, the minimum is unique. This particular case may find applications in processes to determine the stopping power of specific materials such as metal implants, for instance. With this aim in mind, a graphical interface was added to our proton radiography module in openREGGUI. It relies on the optimization formalism proposed by Collins-Fekete (Eq. 7.6) but it gives additional control to the user. It can select the points of the calibration curve to be adapted, as shown in Fig. 7.8. Moreover, it may select specific spots among the data. This is useful because of the strong correlation existing between the presence of lateral inhomogeneities and WEPL estimation inaccuracies [18, 13]. One might want not to consider such areas for the optimization. Up to this day, the input WEPL is determined from a comparison with simulated IDDs. In a future improved version, it could benefit from the deconvolution method discussed in Chapter 6.

Finally, the benefit of proton radiography could be questioned with regards to the issue of establishing patient specific calibration curves. It results from the present study that proton radiography cannot be considered yet as an efficient technique to improve RSPs estimation. Nonetheless, its application on patient would enable the quantification of range errors and therefore permit treatment margin optimization. Moreover, recent studies have shown that the use of dual energy computed tomography (DECT) instead of single energy computed tomography (SECT) for treatment planning could significantly decrease the uncertainty in the RSPs prediction. Taasti *et al.* showed a median difference of 1.9 mm (1.5 %) between the WEPLs of eight patients of whom the RSP were computed based on a DECT on the one hand and on a SECT on the other hand [47]. Furthermore, another study theoretically demonstrated the over-evaluation of the uncertainty associated to the mean excitation

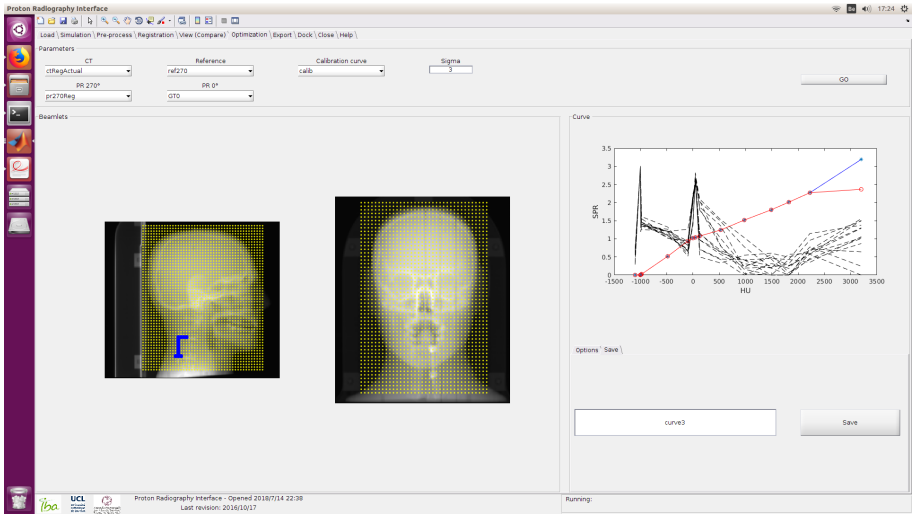

Figure 7.8: Capture of the graphical interface implemented in the openREGGUI framework to patient specifically optimize calibration curves. The optimization of the generic calibration curve (in blue) for the point corresponding to titanium led to the curve shown in red. The spots in blue (on the left panel) were chosen by the user to create the WEPL vector.

energies of tissues which intervene in the RSP computation [50]. Several experimental investigations have been conducted to assess these theoretical hypotheses but were pretty limited because of the lack of suitable systems to acquire range data. Recently, Michalak *et al.* [32] showed a better estimation of RSPs computed based on DECT using range measurements. However, those were only carried out on homogeneous phantoms. More recently, Wohlfart *et al.* [55] performed a similar assessment on an anthropomorphic phantom having a complex geometry but the ground truth stopping power map was based on a high resolution CT and on a table of reference RSP values measured on homogeneous areas of the phantom using a range probe. Consequently, the ground truth map of RSPs cannot be considered as perfectly independent on the CT. In view of the potential significance of DECT for treatment planning accuracy, it is striking that no direct high resolution assessment on patients having a complex geometry has been performed up to this day.

With a spatial resolution equivalent to the one of a planning CT and a submillimeter accuracy on the measured range, the proton radiography methods developed in this thesis could be used to perform such *in vivo* assessment. More generally, proton radiography paves a way to a better assessment of CT calibration by permitting measurements on animal or human tissues.

7.5 Conclusions

Three methods have recently been proposed to optimize the conversion from HUs to RSPs using range data. Thus far, it was believed by some medical physicists that such a patient specific optimization would decrease the range uncertainty. In this paper, we showed that the optimization problem may likely be ill-posed in clinical conditions. This, of course, depends on the geometry and on the acquisition parameters such as the spots positions. This was clearly the case for the head phantom and its associated proton radiograph considered in the present study. Hence, care should be taken if such optimization method were to be applied on patients.

Furthermore, the range uncertainty problem is more complex than just differences existing between the patient's ideal curve and the generic one implemented in the TPS. The piecewise linear model is a restriction itself since the relationship between HU and RSP is actually non bijective. It is worth noting that multi-energy CT (of which the most basic and commonly found form is dual energy CT) might be part of the solution to this issue by providing data acquired with distinct x-ray spectra. However, despite an increasing number of studies, its advantage in the quest for a solution to the unicity issue of the conversion to RSP must be further investigated [17]. In this context, proton radiography with a multi-layer ionization chamber appears as an intriguing option. Offering a spatial resolution equivalent to the one of a planning CT and a submillimeter resolution on the measured range, it could be used to validate CT conversion on animal or human tissues having complex geometries.

Chapter 8

Discussion and conclusion

Proton therapy has the potential to confine most of the dose to the target. Unfortunately, range computation during treatment planning is tainted by various uncertainties, a major source of which arises from the conversion of Hounsfield units (HU) to stopping powers. Despite this being known for decades, there is still a remarkable lack of related experimental data and of method to obtain them. Moreover, recent works [15, 10, 4] have brought to light that the difference between range measurements and predictions made with the calibration curve used for treatment planning could serve as an objective function to optimize the conversion of the Housnfield units (HU) of the planning CT to relative proton stopping powers (RSPs). To better quantify range uncertainty and to potentially correct it, it is necessary to develop techniques to measure high resolution range maps of protons going through a patient. In this thesis, we developed an acquisition process to obtain such range maps and we discussed its applications without hesitating to question the admitted hypotheses on the use of range measurements to generate patient specific calibration curves.

Design of a proton radiography system for clinical use of proton therapy

The six first chapters of this thesis were focusing on the design of a proton radiography acquisition process and post-processing methods to obtain range error maps with a clinically acceptable accuracy. This

work was a straight continuation of the acquisition technique relying on a multi-layer ionization chamber (MLIC) first proposed by Farace *et al.* [19]. In collaboration with these authors, several novel tools were developed.

To begin with, we proposed a first method to generate range error maps that could be used in the context of CT conversion assessment. A fast and direct ray-tracing algorithm was implemented to simulate integral depth dose profiles (IDD) of which the comparison with data measured with a MLIC led to an estimation of the range error. The validity of the method was assessed against both analytical and Monte Carlo dose calculation of our TPS. Our algorithm relying on a direct ray-tracing appeared to be faster and surprisingly more accurate than TPS computation when modeling lateral inhomogeneities. This IDD model was at the core of two additional post-processing methods which are discussed later.

In this preliminary study, a commercial MLIC, the Giraffe (IBA, Belgium) was used and important limitations were highlighted. First, the acquisition time of twenty minutes was too long for common clinical use. Secondly, we showed a high sensitivity of range error maps to residual set-up errors which must be mitigated before they could be used for CT conversion assessment.

To develop faster proton radiography, a larger detector would be desirable. In order to validate the possibility to build such a device, a large field-of-view MLIC was designed and implemented. To limit production costs, a different type of electrode coating was proposed and tested.

To mitigate the potential presence of residual set-up errors, a specific registration method between an x-ray CT and proton radiographs was developed. It relies on the direct ray-tracing method to compute a cost function of which the optimization yields to the best alignment between a CT and proton radiographs. The robustness of the method was studied with respect to measurement noise and calibration errors. The accuracy appeared to be better than 0.3° for angles and 0.3 mm for translations.

The last post-processing method developed in this thesis performs a deconvolution of measured IDDs to better estimate the underlying water equivalent path length (WEPL) of the patient. It also relies on the direct ray-tracing algorithm to compute a cost function which ben-

efits from the fact that the measured curves contain more information than single value pixels. The overall problem is solved in the context of sparse optimization. An asset of the method is its capability to increase the spatial resolution. We could thereby estimate WEPL maps with a submillimeter accuracy and a pixel size of 1×1 mm^2 from proton radiographs acquired with a spot spacing of 6 mm maximum.

Interestingly, 6 mm appeared to be the maximum allowable spot spacing with respect to both WEPL estimation and registration accuracies. This is a paramount parameter in proton radiography since it is linked to the delivered dose. The previous results thus indicate that the dose could be decreased by thirty-six while maintaining the same quality of range error assessment.

Together, these tools can be used to determine the WEPL with a sub-millimeter accuracy and a spatial resolution equivalent to the one of the planning CT, hence permitting accurate assessment of range uncertainty. All the post-processing methods developed in this thesis were implemented in an openREGGUI module so that it could be possible to make them available to proton therapy centers to achieve first clinical trials.

CT conversion optimization with proton radiography

Several authors have proposed optimization methods to solve the issue of range uncertainty arising from the conversion of the planning CT into RSP [15, 10, 4]. Those techniques aiming at generating patient specific calibration curves were reviewed in Chapter 7. Unfortunalty, we brought to light important limitations that were not considered by their authors. Namely, depending on the anatomy and the spots map used for the acquisition, the problem might be ill-posed and the solution might be extremely sensitive to measurement noise and to slight changes in the anatomy of the patient. Nonetheless, for specific materials, such as metal implants, the corresponding part of the calibration could be adapted in a robust manner. This offers the possibility to treat through artificial materials with an increased confidence on the range value.

The results presented in chapter 7 question the potential of proton radiography to reduce the range uncertainty arising from the CT conversion. Moreover, recent studies showed that the use of dual energy computed tomography (DECT) for treatment planning could significantly

increase the accuracy in the RSP estimation [17]. Nonetheless, these studies would benefit from an *in vivo* validation. Since the lack of suitable range verification method, this is currently almost impossible, yet limited attempts have been done [32, 55, 47]. The work presented in this thesis fill this gap by proposing a radiography technique that could be used to perform direct measurements on samples that could be non synthetic and non-uniform. More generally, if offers a way to better assess the calibration of CT scanners used in proton therapy facilities by offering testing possibilities on samples closer to a patient anatomy.

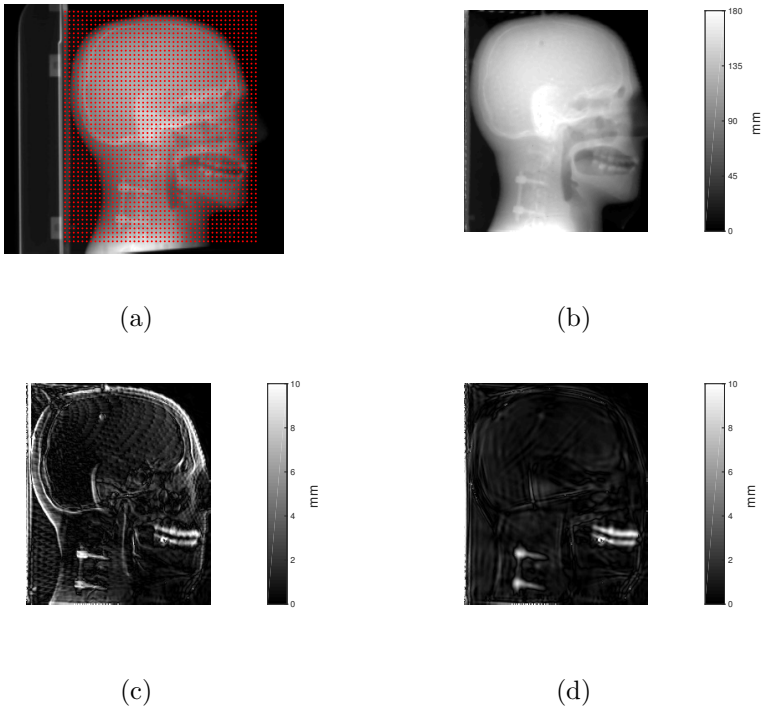

(a) (b)

(c) (d)

Figure 8.1: Range uncertainty assessment based on a proton radiograph of a head phantom acquired with (a) a spot spacing of 5 mm from which (b) a WEPL map was estimated and then (c) compared with the one predicted using the same calibration curve as the TPS. Residual set-up errors can be mitigated using a specific registration method (d).

Fig. 8.1 illustrates the application of the methods developed in this thesis to assess CT conversion errors and suggests a potential workflow to validate CT calibration. In Fig. 8.1a, a proton radiograph was acquired with a spot spacing of 5 mm using a Giraffe. In Fig. 8.1b, a high resolution WEPL map (pixel size 1×1 mm^2) was estimated using the deconvolution algorithm. In other words, the spatial resolution was increased by 25 with respect to the spots map. In Fig. 8.1c, the WEPL map was compared with the one estimated from a CT converted to relative stopping powers (RSP) using the same conversion as the TPS. A residual setup error is observed. Applying our dedicated registration method before the deconvolution, we obtained the WEPL error map shown in Fig. 8.1d where impacts of misalignment can not be seen anymore. In the case of this head phantom, the WEPL error map shows wrong estimation of the RSP of a metal implant attached to vertebrae and of the teeth.

Other perspectives

Many uncertainties intervene in proton therapy. In addition to those taking place during treatment planning, changes in anatomy between fractions, organ motions and residual setup errors contribute greatly to the range uncertainty. To take them into account, more elaborated planning strategies must be adopted. Typically, an optimization is performed on several scenarios to determine the parameters that will give the highest robustness to the plan with respect to the variations mentioned above [46]. Nonetheless, an increase in the robustness generally comes at the cost of the irradiation of a larger volume and a trade-off involving the dose conformity must be obtained. In case of substantial changes in the anatomy, it may be required to adapt the treatment plan. This is generally done offline and takes several hours. Recently however, the first online adaptive workflow was incorporated in commercial systems [2]. In this process, a daily cone-beam CT (CBCT) was used to detect anatomy changes and accordingly adapt the treatment plan. Furthermore, increasing efforts are made to develop faster planning tools so that it is most likely that re-planning could be performed online in a near future.

Because proton radiography provides a direct information about the protons range with a high spatial resolution, we may question the role

that it could play in the context of adaptive therapy. In this thesis, we showed that patient alignment could be better performed with proton radiographs rather than x-rays. Interestingly, aligning the patient with the beam used for treatment also removes uncertainties arising from geometric calibration of the x-ray imaging system. Adapting the rigid registration algorithm to detect changes in anatomy could allow such modification assessment in which context re-planning strategies could be elaborated. However, although such non-rigid registration is theoretically feasible, the information would be bi-dimensional and hence would be likely not to outperform CBCT which is increasingly used in proton therapy. Moreover, the proton radiography method that we proposed has no advantage from the point of view of dose nor in-room time compared to CBCT.

The proton imaging technique investigated in this thesis was rapidly chosen to be 2D in order to avoid the pitfalls of not being easily implementable in clinics. In was indeed many times demonstrated that 3D reconstruction algorithms require an accurate estimation of the proton trajectory inside the patient and hence the use of position trackers [44, 39]. Nonetheless, the efficient deconvolution algorithm that we developed to determine the WEPL could be adapted for 3D reconstruction, as a member of the family of iterative reconstruction algorithms which are for instance sometimes used for CBCT reconstructions. This could potentially pave a way for proton computed tomography with much less hardware and data throughput, especially in the light of recent advances enabling simultaneous irradiation and rotation of the gantry around the patient [14]. Nevertheless, the potential improvement in RSP determination would not be worth the proton imaging dose and irradiation time in the light of modern treatment planning methods such as those relying on DECT. Moreover, proton imaging is limited by the maximum energy that can be provided by the accelerator. If it is generally enough to go through a human head whatever the gantry angle, it is likely not the case for other anatomical sites which enormously limit proton computed tomography applications.

Final conclusion

Proton therapy has the potential to spare healthy tissues better than conventional radiation therapy. However, this promise is currently lim-

ited by uncertainties arising during treatment planning. A better quantification of range uncertainty would help optimize the dose delivered to healthy organs. To achieve this objective, we proposed a proton radiography technique and a set of post-processing methods that we demonstrated to be clinically acceptable both from a practical point of view and in term of accuracy. Nevertheless, we brought to light that proton radiography would generally not be suitable to improve planning CT conversion. Moreover, recent studies have demonstrated the superiority of DECT over SECT for RSP prediction. Consequently, it is most likely that DECT will become the preferred modality for treatment planning in a close future. Nonetheless, quantification of this increase in range certainty would benefit from *in vivo* validations which are still missing. The radiography technique proposed in this thesis is suitable to perform such analysis. It offers a very practical way to assess on patients or on heterogeneous phantoms any method aiming at predicting RSPs.

Finally, the conversion of the planning CT to RSPs is only one, yet a major contribution to the range uncertainty. Achieving the full potential of proton therapy requires to consider all contributions simultaneously. Combining better certainty in RSPs estimation with online adaptive workflows and more flexible delivery techniques will greatly help reach this goal.

Appendices

Appendix A

Mathematical proofs

A.1 Perturbation of the independent term of an over-determined system

Consider the following least-square problem:

$$||\boldsymbol{A}\boldsymbol{x} - \boldsymbol{b}||_2^2 \tag{A.1}$$

where $\boldsymbol{A} \in \mathbb{R}^{m \times n}$ with $m > n$ and $\boldsymbol{b} \in \mathbb{R}^m \setminus \{0\}$.

Matrix $\boldsymbol{A}$ may be expressed through a singular value decomposition:

$$\boldsymbol{A} = \boldsymbol{U}\boldsymbol{S}\boldsymbol{V}^* \tag{A.2}$$

where $\boldsymbol{U}$ and $\boldsymbol{V}$ are unitary matrices and $\boldsymbol{S}$ is a diagonal matrix of which the diagonal elements are the singular values of $\boldsymbol{A}$. If the number of non-zero singular values is n, then the solution to problem A.1 is unique and is given by:

$$\boldsymbol{x}^{\boldsymbol{opt}} = \boldsymbol{A}^+\boldsymbol{b} \tag{A.3}$$

where $\boldsymbol{A}^+ = (\boldsymbol{A}^*\boldsymbol{A})^{-1}\boldsymbol{A}^*$ is the generalized inverse matrix.

Consider perturbations, named $\boldsymbol{\delta b}$, of the independent term. The solutions becomes:

$$\boldsymbol{x}^{\boldsymbol{opt}} + \boldsymbol{\delta x}^{\boldsymbol{opt}} = \boldsymbol{A}^+(\boldsymbol{b} + \boldsymbol{\delta b}) \tag{A.4}$$

We have

$$||\boldsymbol{\delta x}^{\boldsymbol{opt}}||_2 \leq |||\boldsymbol{A}^+||| \; ||\boldsymbol{\delta b}||_2 \tag{A.5}$$

where $|||.|||$ is the operator norm defined as:

$$|||\boldsymbol{A}||| = \sup_{\boldsymbol{x}\in\mathbb{R}^n\setminus\{0\}} \frac{||\boldsymbol{A}\boldsymbol{x}||_2}{||\boldsymbol{x}||_2} \tag{A.6}$$

Moreover,

$$||\boldsymbol{x}^{\boldsymbol{opt}}||_2 = ||\boldsymbol{A}^+\boldsymbol{b}||_2 \tag{A.7}$$

Hence,

$$\frac{||\boldsymbol{\delta x}^{\boldsymbol{opt}}||_2}{||\boldsymbol{x}^{\boldsymbol{opt}}||_2} \leq \frac{|||\boldsymbol{A}^+|||\ ||\boldsymbol{\delta b}||_2}{||\boldsymbol{A}^+\boldsymbol{b}||_2} = \frac{|||\boldsymbol{A}^+|||\ ||\boldsymbol{b}||_2}{||\boldsymbol{A}^+\boldsymbol{b}||_2}\frac{||\boldsymbol{\delta b}||_2}{||\boldsymbol{b}||_2} \tag{A.8}$$

A.2 Perturbation of matrix $\boldsymbol{A}$

Consider the following least-square problem:

$$||(\boldsymbol{A}+\boldsymbol{\delta A})\boldsymbol{x}-\boldsymbol{b}||_2^2 \tag{A.9}$$

where $\boldsymbol{A}\in\mathbb{R}^{m\times n}$ with $m>n$, $\boldsymbol{\delta A}\in\mathbb{R}^{m\times n}$ and $\boldsymbol{b}\in\mathbb{R}^m\setminus\{0\}$.

If the number of non-zero singular values is n, then the solution to problem A.9 is unique and is given by:

$$\boldsymbol{x}^{\boldsymbol{opt}}+\boldsymbol{\delta x}^{\boldsymbol{opt}} = (\boldsymbol{A}+\boldsymbol{\delta A})^+\boldsymbol{b} \tag{A.10}$$

We have

$$\begin{aligned}
\boldsymbol{\delta x}^{\boldsymbol{opt}} &= (\boldsymbol{A}+\boldsymbol{\delta A})^+\boldsymbol{b} - \boldsymbol{x}^{\boldsymbol{opt}} \\
&= (\boldsymbol{A}+\boldsymbol{\delta A})^+\boldsymbol{b} - \boldsymbol{A}^+\boldsymbol{b} \\
&= \boldsymbol{A}^+((\boldsymbol{I}+\boldsymbol{\delta A}\boldsymbol{A}^+)^+ - \boldsymbol{I})\boldsymbol{b}
\end{aligned} \tag{A.11}$$

$$\begin{aligned}
||\boldsymbol{\delta x}^{\boldsymbol{opt}}||_2 &= |||\boldsymbol{A}^+|||\ |||((\boldsymbol{I}+\boldsymbol{\delta A}\boldsymbol{A}^+)^+ - \boldsymbol{I})|||\ ||\boldsymbol{b}||_2 \\
&\leq |||\boldsymbol{A}^+|||\ \frac{|||\boldsymbol{\delta A}\boldsymbol{A}^+|||}{1-|||\boldsymbol{\delta A}\boldsymbol{A}^+|||}\ ||\boldsymbol{b}||_2 \\
&\leq \frac{|||\boldsymbol{A}^+|||^2\ |||\boldsymbol{A}|||}{1-|||\boldsymbol{\delta A}\boldsymbol{A}^+|||}\ \frac{|||\boldsymbol{\delta A}|||}{|||\boldsymbol{A}|||}\ ||\boldsymbol{b}||_2 \\
&\quad , \text{ if } |||\boldsymbol{\delta A}||| < \frac{1}{|||\boldsymbol{A}^+|||}
\end{aligned} \tag{A.12}$$

Moreover,

$$||\boldsymbol{x}^{\boldsymbol{opt}}||_2 = ||\boldsymbol{A}^{+}\boldsymbol{b}||_2 \tag{A.13}$$

Hence,

$$\frac{||\boldsymbol{\delta x}^{\boldsymbol{opt}}||_2}{||\boldsymbol{x}^{\boldsymbol{opt}}||_2} \leq \frac{|||\boldsymbol{A}^{+}|||^2\ |||\boldsymbol{A}|||}{1 - |||\boldsymbol{\delta A}\boldsymbol{A}^{+}|||}\ \frac{||\boldsymbol{b}||_2}{||\boldsymbol{A}^{+}\boldsymbol{b}||_2}\ \frac{|||\boldsymbol{\delta A}|||}{|||\boldsymbol{A}|||} \tag{A.14}$$

Appendix B

Drawings

Section intentionally removed from the online version.

Bibliography

[1] Protonvda inc.: Executive summary. https://www.protonvda.com/. Accessed: 2018-11-06.

[2] Raysearch and iba to demonstrate first online adaptive proton workflow at estro. https://www.raysearchlabs.com/media/press/2018/raysearch-and-iba-to-demonstrate-first-online-adaptive-proton-workflow-at-estro/. Accessed: 2018-04-16.

[3] Low Daniel A., Harms William B., Mutic Sasa, and Purdy James A. A technique for the quantitative evaluation of dose distributions. *Medical Physics*, 25(5):656–661, 1998.

[4] Jaroslav Albert, Rudi Labarbe, and Edmond Sterpin. A method to optimize patient specific hu-sp calibration curve from proton range measurements. *Submitted*, 2018.

[5] Pedro Andreo. On the clinical spatial resolution achievable with protons and heavier charged particle radiotherapy beams. *Physics in Medicine and Biology*, 54(11):N205, 2009.

[6] Michael B. Barton, Susannah Jacob, Jesmin Shafiq, Karen Wong, Stephen R. Thompson, Timothy P. Hanna, and Geoff P. Delaney. Estimating the demand for radiotherapy from the evidence: A review of changes from 2003 to 2012. *Radiotherapy and Oncology*, 112(1):140–144, Jul 2014.

[7] El H Bentefour, Roland Schnuerer, and Hsiao-Ming Lu. Concept of proton radiography using energy resolved dose measurement. *Physics in Medicine and Biology*, 61(16):N386, 2016.

[8] Hans Bischel and Takeshi Hiraoka. Energy loss of 70 mev protons in elements. *Nuclear Instruments and Methods in Physics Research Section B: Beam Interactions with Materials and Atoms*, 66(3):345 – 351, 1992.

[9] S Brousmiche, K Souris, J Orban de Xivry, J A Lee, B Macq, and J Seco. Combined influence of ct random noise and hu-rsp calibration curve nonlinearities on proton range systematic errors. *Physics in Medicine and Biology*, 62(21):8226, 2017.

[10] C-A Collins-Fekete, S Brousmiche, D C Hansen, L Beaulieu, and J Seco. Pre-treatment patient-specific stopping power by combining list-mode proton radiography and x-ray ct. *Physics in Medicine and Biology*, 62(17):6836, 2017.

[11] A. M. Cormack. Representation of a function by its line integrals, with some radiological applications. *Journal of Applied Physics*, 34(9):2722–2727, 1963.

[12] S Deffet, B Macq, R Righetto, F Vander Stappen, and P Farace. Registration of pencil beam proton radiography data with x-ray ct. *Medical Physics*, 44(10):5393–5401, 2017.

[13] Sylvain Deffet, Benoit Macq, Francois Vander Stappen, and Paolo Farace. Water equivalent thickness estimation via sparse deconvolution of proton radiography data. In *2018 IEEE International Conference on Acoustics, Speech and Signal Processing (ICASSP)*, 2018.

[14] Xuanfeng Ding, Xiaoqiang Li, J. Michele Zhang, Peyman Kabolizadeh, Craig Stevens, and Di Yan. Spot-scanning proton arc (sparc) therapy: The first robust and delivery-efficient spot-scanning proton arc therapy. *International Journal of Radiation Oncology*Biology*Physics*, 96(5):1107 – 1116, 2016.

[15] P J Doolan, M Testa, G Sharp, E H Bentefour, G Royle, and H-M Lu. Patient-specific stopping power calibration for proton therapy planning based on single-detector proton radiography. *Physics in Medicine and Biology*, 60(5):1901, 2015.

[16] D Emfietzoglou, R Garcia-Molina, I Kyriakou, I Abril, and H Nikjoo. A dielectric response study of the electronic stopping power of liquid water for energetic protons and a new i -value for water. *Physics in Medicine and Biology*, 54(11):3451, 2009.

[17] Bär Esther, Lalonde Arthur, Royle Gary, Lu Hsiao-Ming, and Bouchard Hugo. The potential of dual-energy ct to reduce proton beam range uncertainties. *Medical Physics*, 44(6):2332–2344, 2017.

[18] P Farace, R Righetto, S Deffet, A Meijers, and F Vander Stappen. Technical note: A direct ray-tracing method to compute integral depth dose in pencil beam proton radiography with a multilayer ionization chamber. *Medical Physics*, 43(12):6405–6412, 2016.

[19] P Farace, R Righetto, and A Meijers. Pencil beam proton radiography using a multilayer ionization chamber. *Physics in Medicine and Biology*, 61(11):4078, 2016.

[20] Emmanouil Fokas, Gerhard Kraft, Hanxiang An, and Rita Engenhart-Cabillic. Ion beam radiobiology and cancer: Time to update ourselves. *Biochimica et Biophysica Acta (BBA) - Reviews on Cancer*, 1796(2):216 – 229, 2009.

[21] K M Hanson, J N Bradbury, R A Koeppe, R J Macek, D R Machen, R Morgado, M A Paciotti, S A Sandford, and V W Steward. Proton computed tomography of human specimens. *Physics in Medicine and Biology*, 27(1):25, 1982.

[22] ICRU. Tissue substitutes in radiation dosimetry and measurement. *ICRU Report*, 44, 1989.

[23] ICRU. Stopping power and ranges for protons and alpha particles. *ICRU Report*, 49, 1993.

[24] Punnoose J., Xu J., Sisniega A., Zbijewski W., and Siewerdsen J. H. Technical note: spektr 3.0—a computational tool for x-ray spectrum modeling and analysis. *Medical Physics*, 43(8Part1):4711–4717, 2016.

[25] Joseph F. Janni. Energy loss, range, path length, time-of-flight, straggling, multiple scattering, and nuclear interaction probability: In two parts. *Atomic Data and Nuclear Data Tables*, 27(2):147 – 339, 1982.

[26] Robert P Johnson. Review of medical radiography and tomography with proton beams. *Reports on Progress in Physics*, 81(1):016701, 2018.

[27] Souris Kevin, Lee John Aldo, and Sterpin Edmond. Fast multipurpose monte carlo simulation for proton therapy using multi- and many-core cpu architectures. *Medical Physics*, 43(4):1700–1712, 2016.

[28] N Krah, M Testa, S Brons, O Jäkel, K Parodi, B Voss, and I Rinaldi. An advanced image processing method to improve the spatial resolution of ion radiographies. *Physics in Medicine and Biology*, 60(21):8525, 2015.

[29] J. Krimmer, D. Dauvergne, J.M. Létang, and É. Testa. Prompt-gamma monitoring in hadrontherapy: A review. *Nuclear Instruments and Methods in Physics Research Section A: Accelerators, Spectrometers, Detectors and Associated Equipment*, 878:58 – 73, 2018. Radiation Imaging Techniques and Applications.

[30] Y. Kumazaki, T. Akagi, T. Yanou, D. Suga, Y. Hishikawa, and T. Teshima. Determination of the mean excitation energy of water from proton beam ranges. *Radiation Measurements*, 42(10):1683 – 1691, 2007.

[31] B Marchand, D Prieels, B Bauvir, R Sépulchre, and M Gérard. Iba proton pencil beam scanning: an innovative solution for cancer treatment. In *2000 EPAC*, 2000.

[32] Gregory Michalak, Vicki Taasti, Bernhard Krauss, Amanda Deisher, Ahmed Halaweish, and Cynthia McCollough. A comparison of relative proton stopping power measurements across patient size using dual- and single-energy ct. *Acta Oncologica*, 56(11):1465–1471, 2017. PMID: 28885130.

[33] S.M. Seltzer J. Chang J.S. Coursey R. Sukumar D.S. Zucker M.J. Berger, J.H. Hubbell and K. Olsen. Xcom: Photon cross sections database. *NIST Standard Reference Database*, 8, 2010.

[34] M Mumot, C Algranati, M Hartmann, J M Schippers, E Hug, and A J Lomax. Proton range verification using a range probe: definition of concept and initial analysis. *Physics in Medicine and Biology*, 55(16):4771, 2010.

[35] Wayne D Newhauser and Rui Zhang. The physics of proton therapy. *Physics in Medicine and Biology*, 60(8):R155, 2015.

[36] W.D Newhauser, U Titt, D Dexheimer, X Yan, and S Nill. Neutron shielding verification measurements and simulations for a 235-mev proton therapy center. *Nuclear Instruments and Methods in Physics Research Section A: Accelerators, Spectrometers, Detectors and Associated Equipment*, 476(1):80 – 84, 2002. Int. Workshop on Neutron Field Spectrometry in Science, Technolog y and Radiation Protection.

[37] H Paganetti. Range uncertainties in proton therapy and the role of monte carlo simulations. *Physics in Medicine and Biology*, 57(11):R99, 2012.

[38] Helmut Paul, Oksana Geithner, and Oliver Jäkel. The influence of stopping powers upon dosimetry for radiation therapy with energetic ions. volume 52 of *Advances in Quantum Chemistry*, pages 289 – 306. Academic Press, 2007.

[39] C T Quiñones, J M Létang, and S Rit. Filtered back-projection reconstruction for attenuation proton ct along most likely paths. *Physics in Medicine and Biology*, 61(9):3258, 2016.

[40] Rescigno Regina, Bopp Cécile, Rousseau Marc, and Brasse David. A pencil beam approach to proton computed tomography. *Medical Physics*, 42(11):6610–6624, 2015.

[41] I Rinaldi, S Brons, O Jäkel, B Voss, and K Parodi. Experimental investigations on carbon ion scanning radiography using a range telescope. *Physics in Medicine and Biology*, 59(12):3041, 2014.

[42] U Schneider, P Pemler, J Besserer, E Pedroni, A Lomax, and B Kaser-Hotz. Patient specific optimization of the relation between ct-hounsfield units and proton stopping power with proton radiography. *Medical Physics*, 32(1):195–199, 2005.

[43] Uwe Schneider, Eros Pedroni, and Antony Lomax. The calibration of ct hounsfield units for radiotherapy treatment planning. *Physics in Medicine and Biology*, 41(1):111, 1996.

[44] Rit Simon, Dedes George, Freud Nicolas, Sarrut David, and Létang Jean Michel. Filtered backprojection proton ct reconstruction along most likely paths. *Medical Physics*, 40(3):031103, 2013.

[45] Pingfan Song, Xin Deng, João F. C. Mota, Nikos Deligiannis, Pier Luigi Dragotti, and Miguel R. D. Rodrigues. Multimodal image super-resolution via joint sparse representations induced by coupled dictionaries. *CoRR*, abs/1709.08680, 2017.

[46] E. Sterpin, A. Barragan, K. Souris, and J.A. Lee. Planification de traitement robuste en protonthérapie. *Cancer/Radiothérapie*, 20(6):523 – 529, 2016. 27e Congrès national de la Société française de radiothérapie oncologique.

[47] Vicki Trier Taasti, Ludvig Paul Muren, Kenneth Jensen, Jørgen Breede Baltzer Petersen, Jesper Thygesen, Anna Tietze, Cai Grau, and David Christoffer Hansen. Comparison of single and dual energy ct for stopping power determination in proton therapy of head and neck cancer. *Physics and Imaging in Radiation Oncology*, 6:14 – 19, 2018.

[48] Scott Tyldesley, Geoff Delaney, Farshad Foroudi, Lisa Barbera, Marc Kerba, and William Mackillop. Estimating the need for radiotherapy for patients with prostate, breast, and lung cancers: Verification of model estimates of need with radiotherapy utilization data from british columbia. *International Journal of Radiation Oncology, Biology, Physics*, 79(5):1507–1515, Apr 2011.

[49] Schneider Uwe and Pedroni Eros. Proton radiography as a tool for quality control in proton therapy. *Medical Physics*, 22(4):353–363, 1995.

[50] De Smet Valérie, Labarbe Rudi, Vander Stappen François, Macq Benoît, and Sterpin Edmond. Reassessment of stopping power ratio uncertainties caused by mean excitation energies using a water-based formalism. *Medical Physics*, 45(7):3361–3370, 2018.

[51] Frederik Jozef Vernimmen and Kathy Rock. Technological progress in radiation therapy for brain tumors. *Journal of Cancer Therapy*, 5:38–43, 2014.

[52] S Webb. The physical basis of imrt and inverse planning. *The British Journal of Radiology*, 76(910):678–689, 2003. PMID: 14512327.

[53] Eric W Weisstein. *Chi Distribution*. MathWorld – A Wolfram Web Resource. Retrieved 1 July 2018.

[54] D. R. White, H. Q. Woodard, and S. M. Hammond. Average soft-tissue and bone models for use in radiation dosimetry. *The British Journal of Radiology*, 60(717):907–913, 1987. PMID: 3664185.

[55] Patrick Wohlfahrt, Christian Möhler, Christian Richter, and Steffen Greilich. Evaluation of stopping-power prediction by dual- and single-energy computed tomography in an anthropomorphic ground-truth phantom. *International Journal of Radiation Oncology * Biology * Physics*, 100(1):244–253, Jan 2018.

[56] H. Q. Woodard and D. R. White. The composition of body tissues. *The British Journal of Radiology*, 59(708):1209–1218, 1986. PMID: 3801800.

[57] M Yang, G Virshup, J Clayton, X R Zhu, R Mohan, and L Dong. Theoretical variance analysis of single- and dual-energy computed tomography methods for calculating proton stopping power ratios of biological tissues. *Physics in Medicine and Biology*, 55(5):1343, 2010.

[58] Ming Yang, X Ronald Zhu, Peter C Park, Uwe Titt, Radhe Mohan, Gary Virshup, James E Clayton, and Lei Dong. Comprehensive analysis of proton range uncertainties related to patient stopping-power-ratio estimation using the stoichiometric calibration. *Physics in Medicine and Biology*, 57(13):4095, 2012.

[59] Indra Yohannes, Daniel Kolditz, Oliver Langner, and Willi A Kalender. A formulation of tissue- and water-equivalent materials using the stoichiometric analysis method for ct-number calibration in radiotherapy treatment planning. *Physics in Medicine and Biology*, 57(5):1173, 2012.